Utrecht University

Master Thesis

Department of Chemistry

Inorganic Chemistry and Catalysis

Colloidal Iron Oxide Nanoparticles supported on Titania as Fischer-Tropsch Catalyst

Author:
W.C. Versluis, BSc

Supervisor:
N. A. Krans, MSc
First examiner:
Prof. dr. ir. K. P. de Jong
Second examiner:
Dr. P. Ngene

February 2018

Utrecht University

Abstract

The attachment of colloidal iron oxide nanoparticles to carbon nanotubes (CNT) and titania supports as Fischer-Tropsch to olefins (FTO) catalysts was investigated. First, 7 nm colloidal iron oxide nanoparticles were synthesized, stabilized by organic ligands. Next, these nanoparticles were deposited on CNT or TiO_2 supports. Moreover, the catalysts were promoted with sodium and sulfur using inorganic ligand exchange. As reference catalysts, incipient wetness impregnation (IWI) was used to deposit iron on the supports where promotors were introduced via co-impregnation. Attaching colloidal iron nanoparticles to the given supports, obtained a narrower particle size distribution and better dispersion than with IWI. The catalysts were tested using a high throughput 16 parallel fixed-bed reactors set-up (Flowrence, Avantium) at industrially relevant conditions. Promotor additions to supported iron on CNT increased the activity and selectivity towards lower olefins and decreased the selectivity towards methane. Interestingly, the promoted iron nanoparticles supported on CNT showed loss of activity at 280 and 300 ℃, indicating a temperature dependent promotion. Promotor additions to supported iron on TiO_2 most probably poisoned the catalysts, because of the inactivity of these catalysts. The activity of unpromoted colloidal iron nanoparticles supported on TiO_2 revealed to be temperature dependent. At 300 ℃, the activity of this catalyst was comparable to colloidal iron nanoparticles supported on CNT at 300 and 340 ℃. Moreover, colloidal iron particles supported on TiO_2 showed higher activity for FTO than catalysts obtained with IWI on TiO_2.

Contents

1 Theory

1.1 Introduction

Lower olefins (C_2 to C_4) are extensively used key building blocks in the chemical industry to produce a wide range of products. Ethylene, propylene, butylene and their derivatives are used to synthesize for example plastics, polymers, cosmetics, drugs, solvents and detergents. [1]

There are several ways to obtain these lower olefins; traditionally from steam cracking of naphtha. Steam cracking is a very energy consuming process and this process to obtain lower olefins contributes to the depletion of oil reserves and emission of CO_2. [2] Therefore there is a need for other routes and feedstocks.

Another way to produce lower olefins is from CO and H_2 (syngas). This route can be divided into two main groups: the indirect processes and the direct processes. [2] In Figure 1 several processes to produce lower olefins from synthesis gas are depicted.

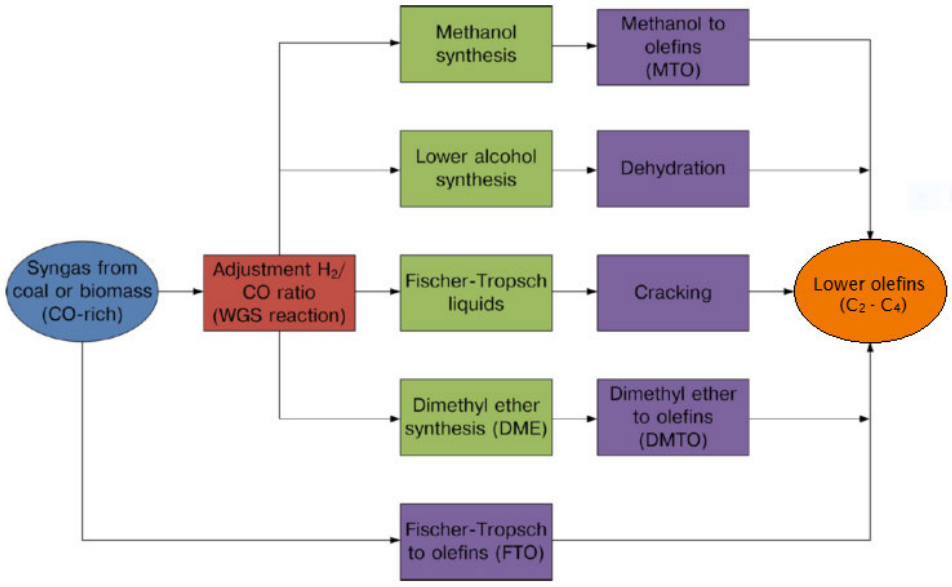

Figure 1: Processes for the transformation of CO-rich synthesis gas into lower olefins. Figure retrieved from *Torres Galvis et al. (2013)*. [2]

Syngas can be produced from biomass, natural gas or coal. The use of biomass as source for synthesis gas is preferred due to it's carbon-neutral nature and low feedstock costs. Products obtained from syngas, as can be seen in Figure 1, are methanol, lower alcohols, Fischer-Tropsch liquids, dimethyl ether and lower olefins (formed direct or indirect). Here, focus lies on the direct conversion of syngas into lower olefins via the Fisher-Tropsch to olefins (FTO) process.

1.2 Fischer-Tropsch to olefins (FTO) reactions

The only metals sufficiently active for FT synthesis are Fe, Co, Ni and Ru. Ruthenium is the most active metal but it is very poisonous and its high cost and low availability are major drawbacks. Nickel produces much more methane (undesired product for FTO) than Co or Fe catalysts and forms volatile carbonyls. Only cobalt and iron catalysts are considered as practical FT catalysts due to their selectivity, low costs and availability. [2] Iron based catalysts are suitable for the high-temperature Fischer-Tropsch (HTFT) process which operates in the 300-350 °C temperature range to produce gasoline and linear low-molecular-mass olefins. Both iron and cobalt based catalysts can be used for the low-temperature Fischer-Tropsch (LTFT) process which operates in the 200-240 °C temperature range to produce high-molecular-mass linear waxes. [3]

Fischer-Tropsch is a complex process but can be simplified into the following reactions [4, 5]:

$$methane : \mathrm{CO} + 3\,\mathrm{H_2} \longrightarrow \mathrm{CH_4} + \mathrm{H_2O} \tag{1}$$

$$\Delta \mathrm{H}^0_{298} = -206\ kJ \cdot mol^-1$$

$$heavier\ hydrocarbons : n\,\mathrm{CO} + 2\,n\,\mathrm{H_2} \longrightarrow (-\mathrm{CH_2}-)_n + n\,\mathrm{H_2O} \tag{2}$$

$$\Delta \mathrm{H}^0_{298} = -154\ kJ \cdot mol^-1$$

$$alcohols : n\,\mathrm{CO} + 2\,n\,\mathrm{H_2} \longrightarrow \mathrm{C}_n\mathrm{H}_{2n+2}\mathrm{O} + (\mathrm{n}-1)\,\mathrm{H_2O} \tag{3}$$

$$\Delta \mathrm{H}^0_{298} = -147\ kJ \cdot mol^-1$$

$$water\ gas\ shift\ (WGS) : \mathrm{CO} + \mathrm{H_2O} \longleftrightarrow \mathrm{CO_2} + \mathrm{H_2} \tag{4}$$

$$\Delta \mathrm{H}^0_{298} = -41\ kJ \cdot mol^-1$$

$$Boudouard\ reaction : 2\,\mathrm{CO} \longrightarrow \mathrm{C} + \mathrm{CO_2} \tag{5}$$

$$\Delta \mathrm{H}^0_{298} = -172\ kJ \cdot mol^-1$$

The Fischer-Tropsch reaction produces hydrocarbons, reaction (2). In this reaction the usage ratio of H_2:CO is 2:1. However, cobalt and iron based catalysts have different product distributions and prefer different usage ratios of H_2:CO. Cobalt catalysts produce more paraffins (see reaction (6)) using an H_2 rich feedstock and iron catalysts produce more α-olefins (see reaction (7)) using a CO rich feedstock. [6] Because of this both catalysts are used for different processes.

$$paraffins\ (Cobalt - based\ catalyst) : (2\,\mathrm{n}+1)\,\mathrm{H_2} + n\,\mathrm{CO} \longrightarrow \mathrm{C}_n\mathrm{H}_{2n+2} + n\,\mathrm{H_2O} \tag{6}$$

$$\Delta \mathrm{H}^0_{298} = -165\ kJ \cdot mol^-1$$

$$olefins\ (Iron - based\ catalyst) : n\,\mathrm{H_2} + 2\,n\,\mathrm{CO} \longrightarrow \mathrm{C}_n\mathrm{H}_{2n} + n\,\mathrm{CO_2} \tag{7}$$

$$\Delta \mathrm{H}^0_{298} = -206\ kJ \cdot mol^-1$$

Reactions (1) and (3) depict the production of undesired products. For cobalt catalysts the water gas shift (WGS) reaction (4) is negligible but for iron catalysts this reaction will approach equilibrium at high temperature FT. The WGS reaction affects the partial pressures (concentrations) of CO, H_2, CO_2 and H_2O which in turn has an impact on the process kinetics. Due to this reaction, iron based catalysts are able to adjust the H_2:CO ratio of the syngas during the process and no additional steps are necessary. [2, 7] Furthermore, CO_2 can be used as reactant due to the reverse WGS which generates CO. [8] The use of CO_2 is preferable, in sight of environmental issues, to remove CO_2 out of the atmosphere.

When only CO is passed over reduced cobalt or iron catalysts at low temperatures (e.g. 220 ℃), chemisorbed carbon monoxide can dissociate in surface carbon, according to the Boudouard reaction (5), and surface oxygen. The surface carbon may agglomerate yielding graphitic carbon or diffuse into the bulk of the metal forming metal carbides, which are shown to form stable phases with iron based catalysts. The surface oxygen can react with adsorbed CO (forming CO_2), diffuse into the bulk of the metal (forming oxide phases (hematite for an iron based atalyst [9])) or react with adsorbed hydrogen when syngas is used (forming surface hydroxyl groups). The removal of surface oxygen is generally assumed to be fast, due to the carbon covered surface. [10]

However, in the presence of syngas cobalt is not carbided and the produced carbon is hydrogenated. In the case of iron, carbidization takes place in the presence of syngas at 220 ℃, but once the carbidization process is completed no further carbon build-up takes place. At high FT temperatures however (e.g. 330 °C), after the formation of iron carbide, deposition of carbon on the iron catalyst continues which causes deactivation, called coking. The carbon deposition rate exceeds the removal rate by hydrogenation. For cobalt catalysts this deactivation process is much less extensive. [4]

1.3 Mechanism

The exact mechanism of the FTO reaction, on a molecular level, is not known yet. Several mechanisms have been proposed and common to all is the assumption that chain growth occurs by a stepwise procedure. [4] The Fischer-Tropsch synthesis is a polymerisation reaction. The monomers for chain growth are produced in-situ from the gaseous reactants hydrogen and carbon monoxide. [10]

The reactants can form a large number of adsorbed species on metal surfaces, which were experimentally observed. The chemisorption of hydrogen gives monoatomic hydrogen, which has a high surface mobility. It is therefore assumed that the adsorption of hydrogen and the reaction with other surface species does not necessarily take place at the same site. [10]

It is assumed that several reaction pathways occur parallel to each other during the FT synthesis, but this is still field of study. All proposed reaction pathways contain four reaction sections [10]:

1. Adsorption of reactants
2. Generation of the chain initiator
3. Chain growth or propagation
4. Chain growth termination or desorption

The four most popular mechanisms are 'alkyl' mechanism, 'alkenyl' mechanism, 'enol' mechanism and 'CO-insertion' mechanism. [10] These mechanisms will be discussed briefly.

The 'alkyl' mechanism (see Figure 2) is the most widely accepted mechanism for chain growth. The surface carbon is hydrogenated into CH, CH_2 and CH_3 surface species. The CH_3 surface species are regarded as chain initiators and the CH_2 surface species as the monomer building blocks for the chain growth. Chain ending, formation of the products, happens via β-hydrogen elimination or hydrogen addition producing primarily α-olefins and n-paraffins respectively. Another way of product formation is the coupling of a surface hydroxyl group with the alkyl chain, forming n-alcohols. This mechanism is developed out of the 'carbide' mechanism.

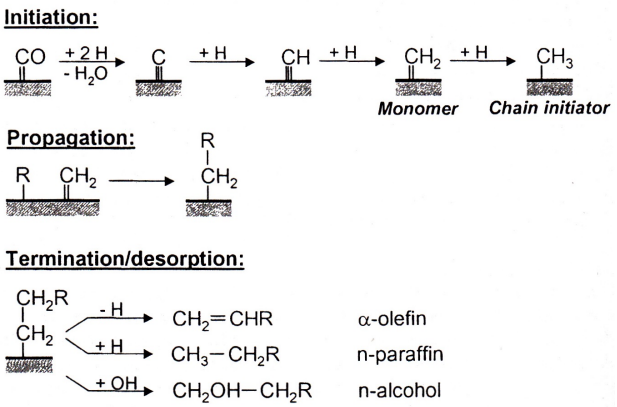

Figure 2: Reaction steps in the Fischer-Tropsch synthesis according to the 'alkyl' mechanism. Figure retrieved from *Claeys et al. (2013)*. [10]

For the 'alkenyl' mechanism (see Figure 3) the hydrogenation of the surface carbon is the same as for the 'alkyl' mechanism. The chain initiator is formed through coupling of CH and CH_2 forming $CH{=}CH_2$ surface species. Also in this mechanism CH_2 is the building block for chain propagation: CH_2 adds to $CH{=}CH_2$ surface species forming surface allyl species. This allyl species isomerize into alkenyl species. The product formation occurs via hydrogen addition to alkenyl species producing α-olefins. An alternative chain growth pathway is required for this mechanism because the formation of n-paraffins is not explained, but when several mechanisms occur this is not necessary.

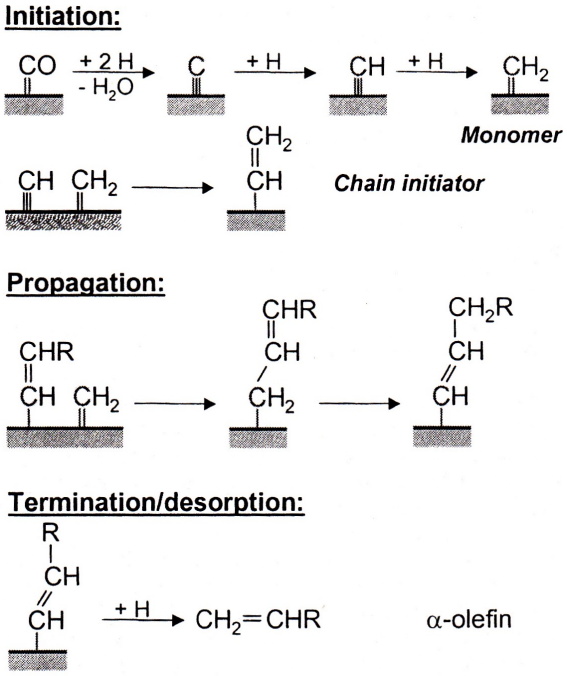

Figure 3: Reaction steps in the Fischer-Tropsch synthesis according to the 'alkenyl' mechanism. Figure retrieved from *Claeys et al. (2013).* [10]

According to the 'enol' mechanism (see Figure 4) CO is hydrogenated to enol surface species. This enol surface species are the chain initiators and the main chain growth monomers. The alternative monomers are formed by hydrogen addition to a enol surface species forming a CH_2OH species. Chain growth then occurs through two routes. First the condensation reaction between two enol species and second the reaction between an enol species and a CH_2OH species, both under addition of hydrogen and under elimination of water. Chain growth termination via hydrogen addition yields alcohols and via desorption yields aldehydes (which can react into acids and esters) and α-olefins (which can be hydrogenated into n-paraffins).

The last mechanism, the 'CO-insertion' mechanism (see Figure 5), is based on the known CO-insertion from coordination chemistry and homogeneous catalysis. The chain initiator is formed via hydrogen addition to CO, forming CH_2OH surface species. Under hydrogen addition and elimination of water methyl CH_3 species are formed, which are the chain initiators. Chemisorbed CO is the chain growth monomer in this mechanism. Insertion of CO-monomers into metal-alkyl bonds yields surface acyl species (CO-R), which form alkyl species under addition of hydrogen and under elimination of water. There are several product formation pathways. Via β-hydrogen elimination from alkyl species α-olefins are formed and from RCHOH species aldehydes are formed. Via hydrogen addition the n-paraffins are formed from alkyl species, aldehydes are formed from acyl species and n-alcohols are formed from RCHOH species.

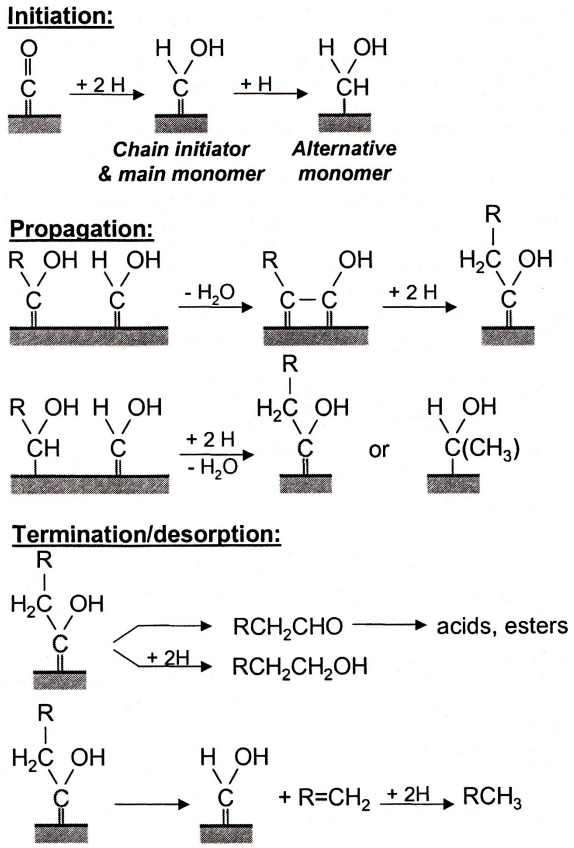

Figure 4: Reaction steps in the Fischer-Tropsch synthesis according to the 'enol' mechanism. Figure retrieved from *Claeys et al. (2013).* [10]

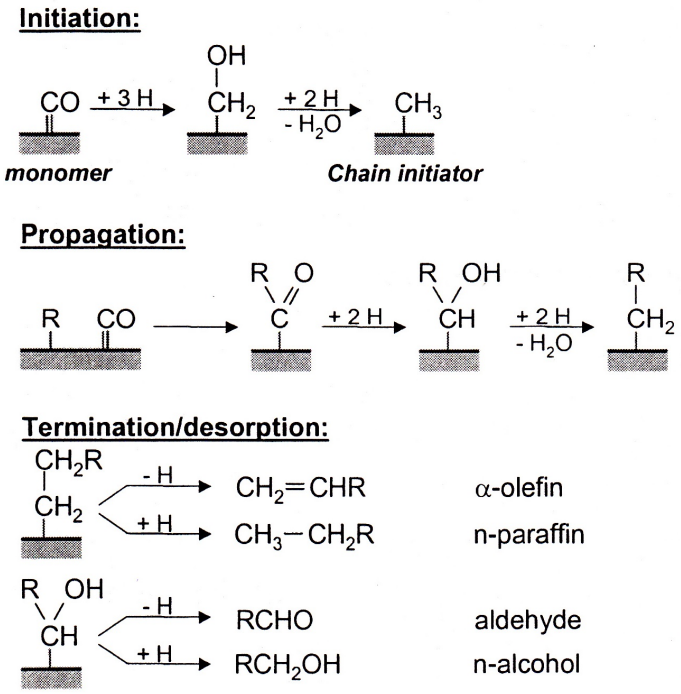

Figure 5: Reaction steps in the Fischer-Tropsch synthesis according to the 'CO-insertion' mechanism. Figure retrieved from *Claeys et al. (2013).* [10]

1.3.1 Activity and selectivity

The activity and selectivity of FTO catalysts are influenced by several catalyst properties and reaction processes. Cobalt and iron based catalysts show different results and react different to catalyst modifications. For example, when iron is deposited on a support material, the formation of the active phase is affected. This formation of the active phase determines the activation of the catalyst and the activity. The adsorption energies of CO and H_2 and the hydrogenation of CO on iron are influenced by the interaction between the metal and the support as well. This influences the reaction rate on the active surface and thus both the selectivity and activity of the catalyst. Also the acidity of the support has influence on the selectivity: increasing acidity produces more C_5+ hydrocarbons. [11] The reaction processes are influenced by several parameters, for example reaction conditions (T, p, GHSV etc.) and the use of promotors. With the use of promotors and adjusting the reaction conditions the activity and selectivity of the iron based catalysts can be tuned. [12]

The reaction processes which affect the activity and selectivity include [12]:

- the diffusion of reactants into and inside a porous catalyst particle to the active sites
- the adsorption of the reactants on the active sites
- chain initiation
- chain growth
- chain termination
- product desorption
- re-adsorption of product with further reaction
- the diffusion of products towards the outside of the catalyst particle

The product distribution of the FTO process can be predicted using the Anderson-Schulz-Flory (ASF) model. This model depends on the chain growth probability α. This parameter α is mainly influenced by reaction conditions, type of catalyst and chemical promoters. According to the ASF model (see Figure 6) an α value between 0.4 and 0.5 obtains the maximum selectivity towards C_2-C_4 olefins. [2] However, optimizing the catalyst and reaction conditions for FTO remains challenging.

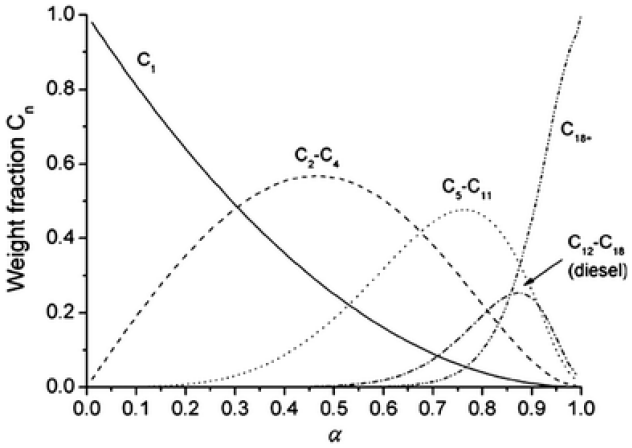

Figure 6: Anderson-Schulz-Flory (ASF) model for the prediction of the product distribution. Figure retrieved from *Smit et al., (2008)*. [13]

1.4 The catalyst

1.4.1 Iron based catalyst

The use of iron based catalysts, with lower FTO activity, over cobalt based catalysts has some major advantages. Iron is less expensive, FT products have a higher olefin content which is desirable for their octane value, it displays a lower methane selectivity at the high temperatures necessary to drive α to lower values (see Figure 6) and iron has a high water gas shift (WGS) activity.

Iron based catalysts have shown promising results. Bulk iron catalysts however are mechanically unstable at high reaction temperatures, which are necessary to obtain a higher product selectivity towards lighter hydrocarbons. At these high temperatures the Boudouard reaction takes place which leads to carbon deposition on the iron and can even break up the catalysts in fragments due to the formation of carbon filaments, see Figure 7. Supported iron catalysts may withstand this mechanical degradation. [1]

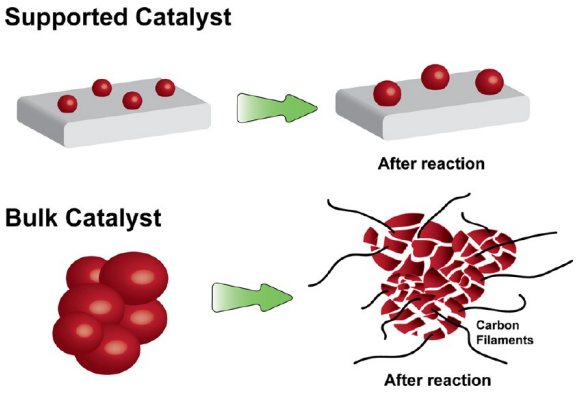

Figure 7: Stabilization of iron-containing nanoparticles on a support. Figure retrieved from *Torres Galvis et al., (2013).* [2]

1.4.2 Active phase

Iron carbide is recognized as the active phase for FTO reactions and not iron in its metallic state. Iron carbide and metallic iron have different CO dissociation barriers and binding strengths for C and O atoms on the surface. The Fe-C bond strength of the carbide phase is weaker than for the Fe metal phase, making desorption of the products possible. This is suggested as reason for the higher activity of iron carbide in the FTO reaction. [14, 15]

The formation of this active phase is affected by the activation energy for iron carbonization, which increases with a decrease in particle size, and the carbonization degree of iron oxides, which is related to the reducibility of the iron oxides. [16] The iron oxide nanoparticles which are deposited on the support first have to be reduced to metallic iron before they can be carbonized to iron carbide. The support and the interaction between the iron particles and the support have influence on the reduction and carbonization of the iron particles. [17]

The low coordination sites at corners and edges of iron carbide particles are the most active. Torres Galvis *et al.* showed with unpromoted iron catalysts supported on carbon nanofibers tested at 1 bar and 350 ℃ with low CO conversion level ($< 1\%$) that all sites are equal in selectivity, and so particle size has minimal influence. Using promotors, only the terrace sites of the iron nanoparticles are influenced. With small particles, where corners and edges dominate the surface, promotors are not effective. So for promoted catalysts an increase in particle size, and thus in terrace sites, has an positive influence on the selectivity towards lower olefins because of the bigger promoted terrace sites surface area. However, the activity decreases with increasing iron carbide particle size. [15]

Unpromoted and promoted iron catalysts were also tested at 20 bar (at 340 ℃) by Torres Galvis *et al.* to assess iron carbide particle size effects on catalytic performance. In the case of unpromoted catalysts, olefin selectivity was low ($< 20\%$c) and accompanied by a high methane selectivity ($> 30\%$c). However for the promoted catalysts, lower olefins selectivity increased with the increase of iron carbide particle size. Furthermore, methane selectivity and activity decreased with increasing particle size. However, for promoted catalysts the activity was five to fifteen times higher than for unpromoted catalysts at 20 bar. [15] For iron particles in the size range of 7 to 20 nm, particle size effects on activity and selectivity seems to be minimal. [1]

1.4.3 Conventional catalyst synthesis methods

Several factors are involved in designing an effective iron based catalyst for the FTO reaction. [2]

- A support with balanced binding strength between the iron particles and the support needs to be obtained to enable the formation of the active phase, enable intimate contact with possible chemical promotors and provide stability
- Effective promotors to increase the selectivity and activity (optional)
- Good wetting of the support for impregnation
- A homogeneous distribution of the iron particles with a narrow size distribution in the optimum size range
- The most optimum process conditions to maximize activity, selectivity and life time of the catalyst

There are three main strategies to deposit nanoparticles on a support: precursor solution impregnation, melt infiltration and deposition of colloidal particles. [18]

Solution impregnation is based on contacting a nanoporous support material with a solution containing a metal precursor. The solution needs to wet the support so that it enters the pores. Oxidic supports are generally easily wetted when using an aqueous precursor solution and filling of the pores by capillary forces is rapid. Carbon-based supports have less good wetting properties and therefore thoroughly drying of the support before impregnation, impregnation under vacuum and/or using a different solvent can be used. Furthermore, the used metal precursor has influence on the deposition of the iron nanoparticles on the support due to the interaction between the metal precursor and the surface of the support. [18]

Based on this interaction, different strategies are used. Most straightforward is impregnation and drying. Incipient wetness impregnation involves the addition of a precursor solution volume equal to the pore volume. After drying a highly dispersed precursor phase is obtained in the pores. During thermal treatment in inert atmosphere or air, the precursor is decomposed and metal oxides are formed. When iron citrate is used as metal precursor a homogeneous distribution of iron over the support is obtained, while using iron nitrate as metal precursor clustering of the iron is observed and nanoparticles are formed. [1, 19]

Another strategy is deposition-precipitation. Here, the support is suspended in a large volume of solution containing the metal precursor and by a controlled change in the pH gradual supersaturation is created. As a result, metal hydroxides precipitate and preferentially nucleate on the suspended support. Small nanoparticles (<10 nm) can be formed, however due to the strong bonding of the particles to the support they are often very difficult to reduce to metallic nanoparticles. [18]

Beside the used metal precursor also the solvent, precursor concentration, support, infiltration procedure and drying procedure strongly influence the final nanoparticle size and particle distribution over the support. Because of this, there is limited control on particle deposition when using precursor solution impregnation techniques. [18, 20]

Melt infiltration is based on infiltration of the support with the pure molten metal or its precursor, which can achieve (almost) complete filling of the pore volume. The nanoporous support is mixed with the metal or precursor and the mixture is heated to above the melting point of the metal or precursor. If there is a good wetting, the pores fill by capillary forces and after cooling and, if relevant, decomposition a nanoconfined solid phase results. This method is only relevant for metals or precursors with relatively low melting temperatures and for the preparation of catalysts with high metal loadings. The melt and support material must be stable under the infiltration conditions and additionally, there is little control on the particle size and distribution over the support. [18]

1.4.4 Colloidal iron nanoparticles

Growth of nanoparticles as colloids in suspension does allow control over particle size as well as over shape and surface. [18, 21–24] By using a colloidal synthesis procedure, where the synthesis and attachment of the metal nanoparticles to the support material is separated, also the control over deposition is enhanced. [23] The particles have a relatively narrow size distribution which excludes particle size dependent results in one catalyst. [15] They consist of an inorganic particle that is coated with a layer of organic ligand molecules and both components can be manipulated independently. [21] In this way the interaction between support and colloids can be tuned. Casavola *et al.* showed that colloidal iron nanoparticles supported on CNT yield relatively sintering-resistant catalysts. [20]

The colloidal synthesis procedure, a bottom-up approach, is based on the model of nucleation and growth, first described by LaMer around 1950. [25] This model can be divided into three parts; stage I, II and III. In stage I the monomer concentration of a certain metal precursor is increasing up to the minimal saturation concentration. When this concentration is reached, stage II starts and nuclei of a critical radius are formed. By the formation of nuclei the monomer concentration decreases, eventually ending up below a critical saturation level. At this point stage II ends and no new nuclei are formed. At last in stage III, the remaining monomers in solution will absorb onto the existing nuclei, which will grow into the final nanoparticles. [26] A sharp transition between stage II and III will increase the final particle size uniformity, in general.

The particles can be synthesized in a 'one-pot synthesis' were all reactions take place in the same reaction mixture. The precursor is quickly injected into the reaction media and a burst in monomer concentration occurs. This injection can be done at relatively high temperatures (100 - 300 °C) in high boiling point apolar solvents, the so-called 'hot-injection' technique. It is also possible to inject the precursor and quickly increase the temperature of the reaction system, the so-called 'heating up' technique. Both techniques ensure a temporally narrow nucleation stage. [21]

Here, the organometallic compound $Fe(CO)_5$ is used as iron precursor for the synthesis of iron oxide nanoparticles. Iron oxide nanoparticles are synthesized in stead of metallic iron particles because of the reactivity and instability. [1] The decomposition of the precursor complex only forms carbon monoxide, whereas other precursors produce a wide range of byproducts. [27] During the thermal decomposition of the complex with the 'heating up' technique, the iron nuclei are stabilized by using ligands to prevent them from aggregation. [28] The final nanoparticles are uniform in size and are stabilized in this way as well, by steric repulsion of the ligands, as can be seen in Figure 8. [24,29]

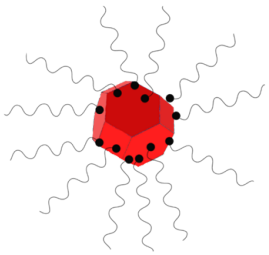

Figure 8: Representation of a colloidal iron oxide nanoparticle, stabilized by organic ligands. Figure adapted from Nag *et al.*. [30]

The iron oxide particle size can be tuned as function of the ligand concentration, however a deep understanding has not been obtained. In general, a larger concentration of ligands in solution enhances the formation of smaller iron particles. [31] For this purpose, the ligands should have a high solubility in organic solvents. Oleic acid, a hydrocarbon chain consisting of 18 carbons with a carboxylic group at C_{18} and a double bond between C_9 and C_{10}, is widely used for this purpose. [31–33] In combination with these oleic acid ligands oleylamine is applied as activating ligand. The oleylamine will react with the acid groups of the oleic acid ligands, forming a small amount of water which accelerates the formation of iron oxides. [20, 27, 34]

Beside the ligands also the solvent has influence on the final iron particle size. Torres *et al.* showed that colloidal iron particles could be synthesized with increasing sizes going from hexadecene to octadecene to docosane as solvent. [1] As organic solvent for this synthesis 1-octadecene is used. It has a relatively high boiling point of 315 °C and it is inert to the iron particles.

As mentioned before, iron oxide nanoparticles are synthesized which are reduced *in situ* to obtain metallic iron particles. When iron is surrounded by five carbonyl ligands, the original metal precursor, it is in a zero valent state. Upon decomposition of the complex several different charged iron species are obtained, mostly Fe^{2+} and Fe^{3+}. [13] By adding a reducing agent to the reaction mixture, Fe^{3+} is reduced to Fe^{2+}. In combination with iron pentacarbonyl as metal precursor, often a mild reducing agent is used. [35] An example of a mild reducing agent is 1,2-hexadecanediol, used in this synthesis.

1.4.5 Metal-support interaction

Support materials are used to optimize and maximize the surface area of the active phase in heterogeneous catalysts and for stabilization of the nanoparticles. Because of this, support materials with a high surface area are preferred. [2] Oxidic supports induce strong metal-support interactions (SMSI) which prevent the particles from sintering. However, these SMSI hinder the conversion of iron oxide into metallic iron and inhibit the formation of the active iron carbide phase. [36] Instead, mixed iron oxides are formed. Iron in iron aluminates and iron silicates is known to be difficult to reduce. A weakly interactive support facilitates the reduction of iron oxides and can facilitate close contact between the iron particles and the possible promotors, but the weak physical binding between the iron particles and the support will not withstand the reaction conditions. Due to this weak binding the particles can sinter severe and form aggregates which lead to an reduction in the active surface area and activity of the catalyst. [2]

TiO_2, as metal oxide support, interacts more severely with the active iron metal than carbon nanotubes. [37] Carbon materials as support induce weak metal-support interactions (WMSI) and sintering of the particles is the main cause of deactivation. Particle growth decreases the active surface area and thereby the activity of the catalyst. However, using carbon materials iron carbide can easily be formed and active catalysts have been obtained.

Titania exists in three crystalline forms; anatase, rutile and brookite. Anatase and rutile are the most common types. In this study commercially available titania, P25, is used which is a mixture of 85 % rutile and 15 % anatase.Due to its non-toxicity, good mechanical resistance and stability in acidic and oxidative environments, titania is widely used for heterogeneous catalysts support. However, some drawbacks include small specific surface areas and low adsorption abilities. [38] The industrially most relevant carbon materials are the 'activated carbons'. These materials have a broad pore size distribution and high specific surface areas. However, for fundamental studies well-defined nanostructured carbons are much more attractive. Carbon nanotubes consist of a graphitic sheet rolled up into a cylindrical tube. They can have a diameter between 2 and 200 nm and a length in the order of micrometers. Multiwalled carbon nanotubes, used in this study, consist of multiple concentric graphitic cylinders. The graphite surface is hydrophobic, where TiO_2 is hydrophilic. Furthermore, graphite has a very low surface energy and therefore WMSI. [39]

The active metal particles bond to the support either through the formation of a surface compound or through electronic exchange with a partially reduced support material. Reduction of the support is due to the close proximity of the active metal and the support and exposure to elevated temperatures. [37, 40, 41] At elevated temperatures, the TiO_2 surface can be reduced to a lower valency (TiO_x *with* $x < 2$) and this TiO_x species then interacts with the active metal surface. This strong TiO_x-metal interactions are difficult to reduce. [41] During catalyst preparation and reduction and oxidation of metallic iron particles also transport of titanium species can occur. [41,42]

The adsorption energies of CO and H_2 on the surface of the active metal are affected by the interactions between the support and the active metal. [41] These energies affect the kinetics and selectivity of the FTO process. The mechanism explaining these changes in the adsorption energies of CO and H_2 is not well understood. [43]

The synthesized iron oxide nanoparticles are completely capped with organic ligands which block the metal active sites during catalysis. By stabilizing the nanoparticles on a support, aggregation is prevented and the ligands can be removed. This ligand removal is done by a thermal annealing procedure where the colloidal particles, a solvent and the support material are mixed and heated to relatively high temperatures. The longer the hydrocarbon ligands, the higher the boiling point and therefore the more challenging to detach the ligands. When the ligands detach, the particles ideally attach to the support with a homogeneous distribution and without change in the particle size or shape. [23, 44]

In order to gain more insight and improve iron based FTO catalysts, colloidal iron particles supported on TiO_2 are studied. The SMSI, which prevent sintering of the particles, in combination with the well defined colloidal particles, which may reduce the formation of mixed iron oxides and enhance iron carbide formation on oxidic supports, are interesting to study.

1.4.6 Promotors

The catalytic properties of FTO catalysts can also be influenced by promotors such as alkali metals, Cu, Zn or V and in this way compensate the influence of the inactive mixed iron oxides. For iron based catalysts mostly sodium and sulfur are used as promotors. [1, 45] Sodium decreases the production of methane, increases WSG activity and facilitates the formation of olefins instead of paraffins. The use of traces of sulfur reduce methane formation even more, weakens Fe-C bonds, thereby increasing the activity, and favors β-hydrogen elimination, which increases the selectivity towards lower olefins. The β-hydrogen elimination is favored by blocking the hydrogenation sides of the catalyst. [46]

Using promotors, the iron carbide size shows significant influence on the selectivity as well. An increase in size (from 2 to 7 nm) shows an increase in selectivity towards lower olefins and an increase in the chain growth probability α. [15] Moreover, the formation of the active phase, iron carbide, is slow in absence of promoters. [36] Furthermore it is suggested that when using Na and S promotors on iron particles, there is less deposition of carbon, which influences the chemical and mechanical stability of the catalyst. [45]

Nag *et al.* showed that long-chain organic capping ligands on chemically synthesized nanocrystals could be replaced with metal-free inorganic ions. These ions adhered to the NC surface in close proximity and provided colloidal stability in polar solvents. [30] Casavola *et al.* used this knowledge to replace the organic ligands on iron NCs supported on CNT with sodium and sulfur via inorganic Na_2S ligand exchange, see Figure 9. By using this strategy, the promotors were directed onto the active metal surface in close proximity and the promotor concentration could be tuned. [47]

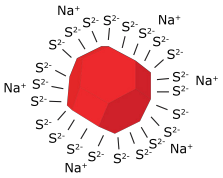

Figure 9: Representation of the result of Na_2S inorganic ligand exchange. Figure adapted from Nag *et al.*. [30]

The exact mechanism is not known and due to the low loadings it remains challenging to determine the exact location of the promotors. It is suggested that the promoters are selectively deposited on the iron particles due to interaction between the iron particles and the promotors, but most likely the promotors end up both on the support and particles. When using incipient wetness impregnation the promotors are introduced on the catalyst by co-impregnation of the promotor precursors. In this way there is very limited control over the distribution of the promotors on the catalyst and most probably end up on both the particles and the support. [47]

1.4.7 Deactivation

There are several deactivation mechanisms for iron based catalysts: poisoning, particle growth, iron phase change by re-oxidation and carbon deposition which blocks the active sites.

Poisoning of the catalyst is mainly due to impurities in the syngas feed, such as oxygen, chlorine, bromine and sulfur. Especially sulfur is reported and is known to decrease the activity of the catalyst when it is present at relative high concentrations (10 ppm). The poisoning effect is due to the oxidizing properties of sulfur, which will affect the active phase iron carbide. [27] When used at relatively low concentrations sulfur is known as promotor. [1, 48] The addition of extra Na and S only increases the activity of the catalyst further until a certain maximum but will not affect the selectivity. [15, 49] However, a too high concentration of any promotor can cause poisoning of the iron catalyst and cause deposition of carbon. [50]

Iron particle growth depends on temperature, metal-support interactions, particle-particle interactions and the way the particles are stabilized, with ligands for example. Growth can occur due to Ostwald ripening or sintering of the particles. [51] However, in order to grow iron surface atoms need to gain mobility. This mobility is gained when the temperature is above the Tamman temperature, which is half of the bulk melting point. For iron this Tamman temperature is 633 °C. This temperature is significantly higher than the reaction conditions for FTO. However, due to the exothermic FTO reaction local hot-spots can develop where the iron is exposed to much higher temperatures compared to the reaction temperature. [52] In combination with the other parameters the amount and rate of growth is determined. Due to particle growth the surface to volume ratio is lowered and as a result the catalytic active surface area is decreased.

Iron phase change is a process which occurs during time on stream. [53] The re-oxidation of iron carbides, the active phase, by water to magnetite, is an important phase change. [7] Water is formed as byproduct during the FT reactions, see section 1.2. The formation of water will decrease the reaction rates of (1), (2) and (3) and increase the WGS reaction (4). Due to the the WGS reaction more CO_2 will be formed and the increased pressures of H_2O and CO_2 will catalyze the formation of inactive iron species. [54]

Carbon deposition, or coke formation, can occur via the Boudouard reaction (see section 1.2, (5)) or the formation of solid or highly viscous products. These product species can block the active sites or decrease the reaction rate. In high temperature FT graphene like carbon species are formed. [13] This carbon formation can only be minimized when hydrogen coverage is high enough due to a total pressure of 20 bar in combination with a high H_2/CO ratio. [55]

2 Methods and Materials

2.1 Catalyst synthesis

The iron was deposited on commercially available carbon nanotubes (CNT) and titania P-25 (TiO_2) with precursor solution incipient wetness impregnation and a colloidal heating-up method, aiming at 3 wt% Fe. All catalysts were promoted aiming at 0.14 wt% sodium and 0.06 wt% sulfur. The precursors used for impregnation were ammonium iron(III) citrate and iron(III) nitrate nonahydrate. All chemicals were used as received.

2.1.1 Incipient wetness impregnation (IWI)

For the synthesis of the impregnated reference catalysts, the procedure was adapted from Torres Galvis *et al.* [45]. Unpromoted 3 wt% Fe on CNT catalysts were synthesized by first obtaining a 0.7 M precursor solution. This was done by dissolving 0.207 g ammonium iron citrate (Fluka, purum p.a., 14.5−16 wt % Fe) or 0.217 g iron nitrate nonahydrate (Acros, ACS reagent $\geq$ 98%) in 0.5 mL demineralized water and 0.25 mL methanol (Aldrich, 99.8 %). The solution was impregnated in a single step on 1.0 g vacuum dried pristine multiwalled carbon nanotubes (Baytubes C 150 HP, Bayer MaterialScience, sieve fraction 212-425 μm) after which the catalysts were dried in static air at 120 ℃ for 2 hours. Calcination was performed at 500 ℃ for 2 hours (5 ℃/min; 100 mL/min for 1 g catalyst) under nitrogen flow and subsequently the catalysts were cooled to room temperature. In a last step passivation was done by increasing oxygen concentration stepwise (2% v/v increase every 30 min) until reaching 20% v/v.

To obtain the promoted 3 wt% Fe on CNT catalysts using IWI, the procedure was adapted from Casavola *et al.* [56]. First a 0.7 M precursor solution with 0.05 M sodium and 0.02 M sulfur was obtained. This was done by dissolving 0.202 g ammonium iron citrate, 0.004 g sodium citrate tribasic dihydrate (Aldrich, $\geq$ 99%) and 0.005 g iron(II) sulfate heptahydrate (Aldrich, $\geq$ 99%) in 0.5 mL demineralized water and 0.25 mL methanol. The other precursor solution consisted of 0.217 g iron nitrate nonahydrate, 0.00517 g sodium nitrate (Acros, ACS reagent $\geq$ 99% and 0.00183 g sulfuric acid (AanalaR Normapur, 95%) and was dissolved in in 0.5 mL demineralized water and 0.25 mL methanol as well. The catalysts were impregnated, dried, calcined and passivated following the procedure described above.

Using TiO_2 (P25, Degussa Evonik Aeroxide, sieve fraction 75-150 μm) as support material for the synthesis of unpromoted and promoted 3 wt% Fe IWI catalysts, the procedure was similar except that the precursors were dissolved in 0.31 mL of demineralized water and the calcination was performed at different temperatures, namely 250, 350 or 500 ℃ for 2 hours. Finally, these catalysts were sieved in the 75-150 μm sieve fraction again.

2.1.2 Colloidal method

The procedure for the colloidal heating-up method and attachment was retrieved from Casavola *et al.* [20]. In a 100 mL three-neck round bottom flask 1.5 mmol (0.43 g) oleic acid (Aldrich, 90%), 0.75 mmol (0.21 g) oleylamine (Aldrich, 70%) and 1.25 mmol (0.35 g) 1,2-hexadecanediol (Aldrich, 90%) were mixed in 10 mL 1-octadecene (Aldrich, 90%). Two openings were closed with a septum and the flask was connected to a Schlenk line through a reflux cooler. The mixture was stirred at 650 rpm at 120 ℃ and degassed (under vacuum) for approximately 30 minutes. Next, the mixture was purged under nitrogen flow. 1 mL 1-octadecene was added to 1 mmol (0.21 g) iron(0) pentacarbonyl (Aldrich, 99.99%). The iron precursor was injected in the cooled down mixture at 90 ℃ and heated to 290 ℃ to reflux for 1 hour under continuous stirring. Finally, the mixture was cooled down to room temperature and further processed in air. The nanocrystal suspension was purified by four cycles of precipitation in isopropanol and redispersion in a few drops of toluene. In the last step, the particles were dispersed in approximately 1 mL toluene. This general procedure produced particles of approximately 7 nm.

Subsequently, the attachment of the iron nanocrystals onto the support was done as follows. 10 mL 1-octadecene was added to the as-synthesized iron nanocrystal solution. A 100 mL three-neck flask was loaded with 800 mg of untreated multiwalled carbon nanotubes (sieve fraction 212-425 μm) or 800 mg TiO_2 (sieve fraction 75-150 μm) and the suspension of iron nanocrystals was injected under stirring at 400 rpm. The solution was degassed (under vacuum) at 120 °C for 15 to 30 minutes and successively heated up to 200 °C under nitrogen flow and stirring. The reaction mixture was kept at this temperature for 30 minutes. Next it was cooled down to room temperature under nitrogen flow without stirring. The catalysts were washed six times with hexane and acetone in a 1:3 ratio. Lastly, the catalysts were dried in static air at 60 °C for 1 hour, at 120 °C for 3 hours and finally under vacuum at 80 °C for 3 hours.

The procedure for promotion of the colloidal iron catalysts using Na_2S inorganic ligand exchange was adapted from Nag *et al.*. [30] to To obtain a 0.05 M stock solution, 0.24 g sodium sulfide nonahydrate (Aldrich, $\geq$ 98%) was sonicated in 20 mL formamide (Aldrich, $\geq$ 99.5%) for 1 h. In order to have a molar ratio of Na_2S:Fe = 1:2, 100 mg of synthesized 3 wt% supported iron catalyst was mixed with 0.54 mL of 0.05 M stock solution and stirred at 400 rpm for 10 minutes. Next the catalysts were washed one time with ethanol, four times with ethanol and acetone (ratio 1:3) and finally one time with acetone. At last, the catalysts were dried at 60 °C for 1 h under static air, 120 °C for 3 h under static air and room temperature for 3 h under vacuum.

2.2 Analysis

Transmission electron microscopy (TEM) or scanning transmission electron microscopy (STEM) and energy-dispersive X-ray spectroscopy (EDX) was used to obtain particle size, particle size distribution and particle distribution of the iron nanocrystals. TEM was performed with a Philips FEI Tecnai 10,12 or 20 operated at 120 kV. STEM and STEM-EDX were performed with a FEI Talos F200x equipped with a super x EDX detector operated at 200 kV. A small drop of the iron NC dispersion or a small scoop of catalyst grains was diluted in 1 mL of toluene and after short sonication, one drop was applied to a Formvar TEM-grid with 200 mesh copper or a Lacey TEM-grid with 300 mesh copper. Particle size analysis was performed with iTem.

X-ray diffraction (XRD) was used to determine the crystal phase and if possible the size of the iron nanocrystals. XRD was performed on a Bruker D2 Phaser.

Inductively coupled plasma - optical emission spectroscopy (ICP-OES) was used to find the weight percentages of iron and Na_2S promotors on the catalysts.

Thermogravimetric analysis and coupled mass spectrometry (TGA-MS) was used to establish the decomposition temperature of the impregnated catalysts to determine an effective calcination temperature. TGA-MS was performed on a PerkinElmer Pyris 1TGA apparatus.

2.2.1 Catalytic tests

The catalysts were tested using a high throughput 16 parallel fixed-bed reactors set-up (Flowrence, Avantium) at industrially relevant conditions for the FTO reaction. Reduction was done at 340 °C for 2 hours with a volume ratio of H_2:He = 1:3, 70 ml/min. Next, carbidization was performed at 280 °C for 10 minutes with a volume ratio of H_2:CO = 2:1, 40 ml/min. Hereafter the reaction ran at 340 °C with a volume ratio of H_2:CO = 2:1, 100 ml/min, GHSV = 3600 h^-1. All steps were at 10 bar. In an other experiment the reaction conditions were adapted to a reduction temperature of 240 °C, carbidization at 240 °C and reaction temperatures of 240, 260, 280 and 300 °C subsequently.

All products of the FTO reaction were analyzed by means of gas chromatography using a Varian CP3800 equipped with a FID detector.

3 Results and Discussion

3.1 Catalyst synthesis

3.1.1 Incipient wetness impregnation

Using incipient wetness impregnation, the iron precursor was directly deposited on the support. After calcination, the resulting catalysts were analyzed. With ICP-AES the weight loading of iron, sodium and sulfur was determined, see Table 1.

The sample names contain the deposition method (i (incipient wetness impregnation) or c (colloidal method)), metal (Fe) and support material (CNT or TiO_2). For the impregnated catalysts also the iron precursor (N (iron nitrate nonahydrate) or C (ammonium iron citrate)) and calcination temperature is denoted. When the catalysts are promoted, 'P' is added after the metal.

Table 1: Catalyst weight loading iron (wt% Fe) and weight loading promoters (wt% Na and wt% S) using IWI, as determined by ICP-AES measurements.

Catalyst	**Weight loading iron (wt% Fe)**	**Weight loading promoters**	
		wt% Na	wt% S
iFe/CNT-C-500	2.5	–	–
iFeP/CNT-C-500	3.0	0.10	0.06
iFe/CNT-N-500-1	3.0	–	–
iFeP/CNT-N-500-1	3.0	0.14	0.04
iFe/CNT-N-500-2	2.7	–	–
iFeP/CNT-N-500-2	2.8	0.13	0.04
iFe/TiO_2-C-500	1.9	–	–
iFeP/TiO_2-C-500	2.1	0.09	–
iFe/TiO_2-C-250	2.5	–	–
iFe/TiO_2-N-350-1	2.7	–	–
iFeP/TiO_2-N-350-1	3.0	0.13	–
iFe/TiO_2-N-350-2	2.7	–	–
iFeP/TiO_2-N-350-2	2.8	0.14	–

Based on Table 1, it is shown that with both iron precursors the iron is deposited on the support materials using IWI. Using CNT as support material the weight loading of iron was around 3 wt%. When using TiO_2 as support material and ammonium iron citrate as precursor, iFe/TiO_2-C-500 and iFeP/TiO_2-C-500, a slightly lower weight loading was obtained of around 2 wt%. However, in a second batch, iFe/TiO_2-C-250, the iron weight loading was in the right range of about 3 wt%. The lower weight loadings were most likely due to the smaller impregnated volumes because of the inaccuracy of the syringes and needles. Furthermore, variation in iron weight loading could be due to an inhomogeneous distribution of the iron on the support material.

Sodium and sulfur promotors were introduced on the catalysts using co-impregnation. The sodium weight loading of all catalysts was in the range of approximately 0.14 wt% Na. On TiO_2 no sulfur seems to be deposited. However, it is challenging to detect sulfur using ICP-AES, especially with low weight loadings, and for that reason the sulfur weight loadings are not reliable.

Using HAADF-STEM and HAADF-STEM-EDX elemental mapping the location, size and shape of the iron oxide particles were verified. In Figure 10 the results of impregnation of the supports with ammonium iron citrate, drying and calcination for 2 hours at 500 °C are depicted, see Figure 10. On CNT relatively small iron oxide particles with sizes between 3 and 25 nm were formed with an average of around 10 nm, which were well dispersed over the support. On TiO_2 relatively big particles with sizes between 25 and 50 nm were formed after calcination, with a poor particle distribution over the support. Beside the big particles also small particles, with sizes below the resolution limit, were formed which could also be a mixed phase between TiO_2 and the iron.

From literature it is known that with ammonium iron citrate as precursor, a layer of iron is formed upon the support instead of particles. [19] This layer can easily integrate into the TiO_2 surface due to the SMSI and form a mixed phase. Moreover, if iFe/TiO_2-C was calcined at 250 ℃, there were no visible particles formed at all, as is indicated in Figure 11. Iron was present but only as small particles, a layer or as a mixed phase with TiO_2.

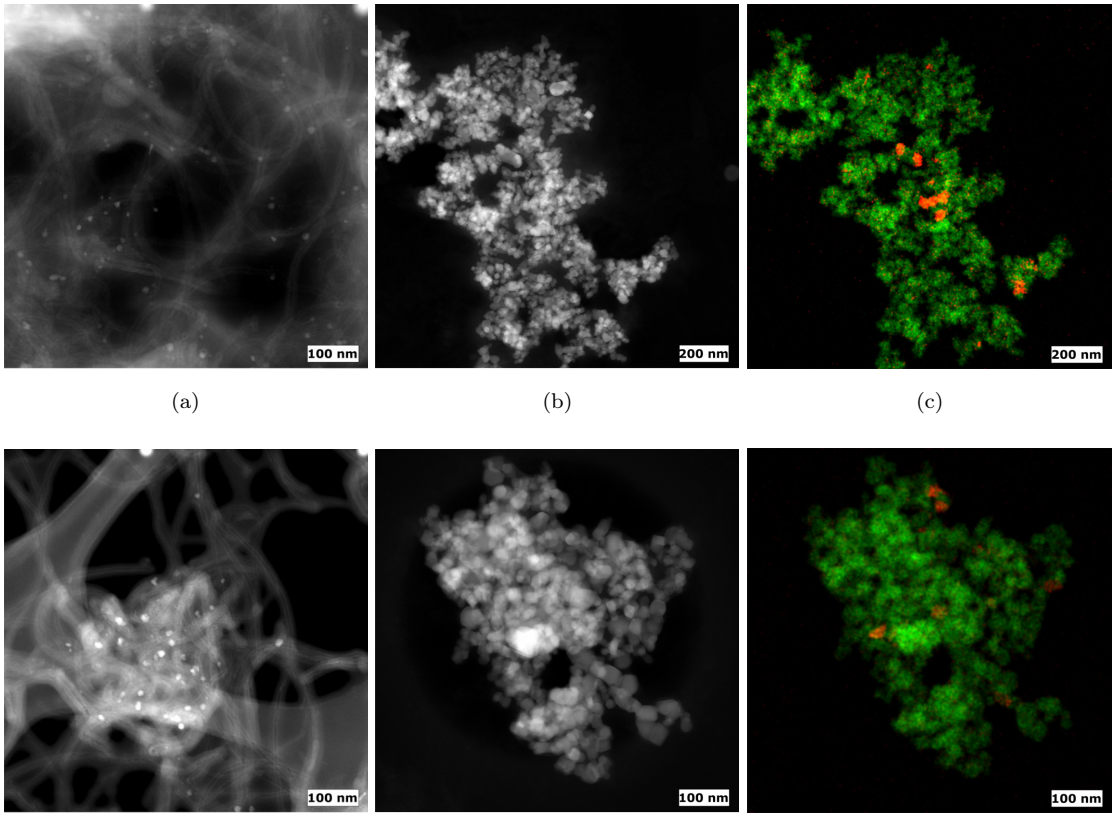

(a) (b) (c)

(d) (e) (f)

Figure 10: HAADF-STEM and HAADF-STEM-EDX images of ammonium iron citrate IWI; (a) iFe/CNT-C-500, (b+c) iFe/TiO_2-C-500, (d) iFeP/CNT-C-500 and (e+f) iFeP/TiO_2-C-500. (c) and (f) are HAADF-STEM-EDX images; green indicates Ti, red indicates Fe.

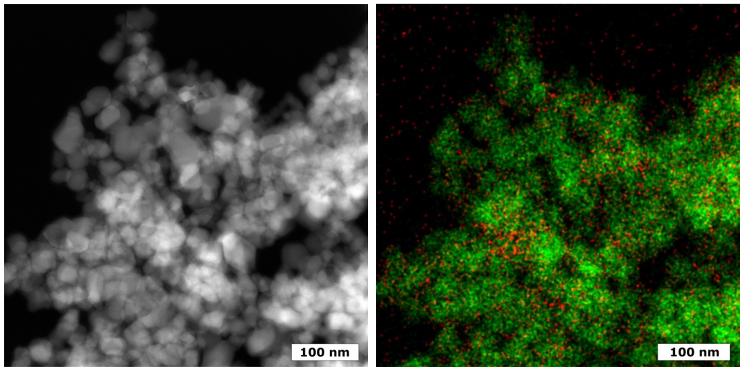

(a) (b)

Figure 11: (a) HAADF-STEM image and (b) HAADF-STEM-EDX image of iFe/TiO_2-C-250. Green indicates Ti, red indicates Fe.

Moreover, TGA-MS was used to study the decomposition of ammonium iron citrate and determine the appropriate calcination temperatures for both supports, see Figure 12. The iron citrate impregnated CNT suffered the biggest weight loss between 200 and 250 ℃ and a gradual decrease between 250 and 500 ℃. A calcination temperature of 500 ℃ is sufficient to decompose the iron precursor and form metallic iron particles. Around 670 ℃ another sharp decrease in weight was observed, which is most probably from the decomposition of the carbon support itself. [57] From the MS data an increase in signal for carbon containing species was found around this temperature, see Figure A.1.

The iron citrate impregnated TiO_2 also had the biggest weight loss between 200 and 250 ℃. From 250 ℃ on there is a constant decrease in weight up to 800 ℃. As for the impregnated CNT, until 450 ℃ this decrease can be ascribed to the decomposition of the iron precursor. However, the constant decrease after 450 ℃ indicated that the support, TiO_2 P25, was not stable at this high temperatures. From literature it is known that calcination above 465 ℃ resulted in a phase transition from anatase to rutile. [38] Part of this phase transition occurred at lower temperatures, probably. To maintain the initial phase ratio of P25, a calcination temperature significantly below 465 ℃ was required. For the total decomposition of the ammonium iron citrate, a temperature of at least 500 ℃ was necessary. However, a calcination temperature of 250 ℃ was used. At this temperature most of the precursor was decomposed, as is indicated by the steep decrease in weight between 200 and 250 ℃ in Figure 12b. For further experiments calcination temperatures between 350 and 450 ℃ are more convenient. At this temperatures the iron precursor is decomposed to a greater extent and more particles are likely to form. Though, to maintain the initial phase ratio of the TiO_2 P25 calcination temperatures between 350 and 400 ℃ are favorable.

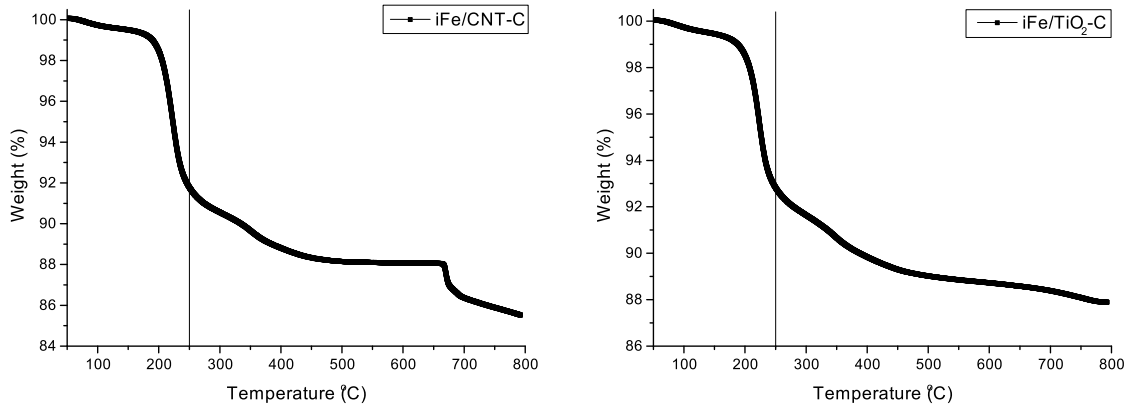

(a) (b)

Figure 12: TGA of the weight loss due to the decomposition of ammonium iron citrate on CNT (a) and TiO_2 (b).

Because of the poor particle formation and distribution on TiO_2 using ammonium iron citrate as precursor, impregnation with iron nitrate nonahydrate was studied. In Figure 13 the results of this impregnation are depicted after drying and calcination for 2 hours at 500 or 350 ℃. On CNT support particles with a broad particle size distribution were formed after calcination. The particles were nicely distributed over the support and had a size between approximately 3 and 20 nm. The average particle sizes were comparable to the colloidal particle sizes and therefore formed a convenient reference. However, on TiO_2 only big particles were formed, with sizes larger than 20 nm and up to 60 nm. Moreover, as for ammonium iron citrate, areas with iron integrated into the TiO_2 support were common, most likely due to the SMSI. In Figure A.2 the TGA of the weight loss due to the decomposition of iron nitrate nonahydrate on TiO_2 is depicted and shows that a calcination temperature of 350 ℃ is sufficient to decompose most of the precursor.

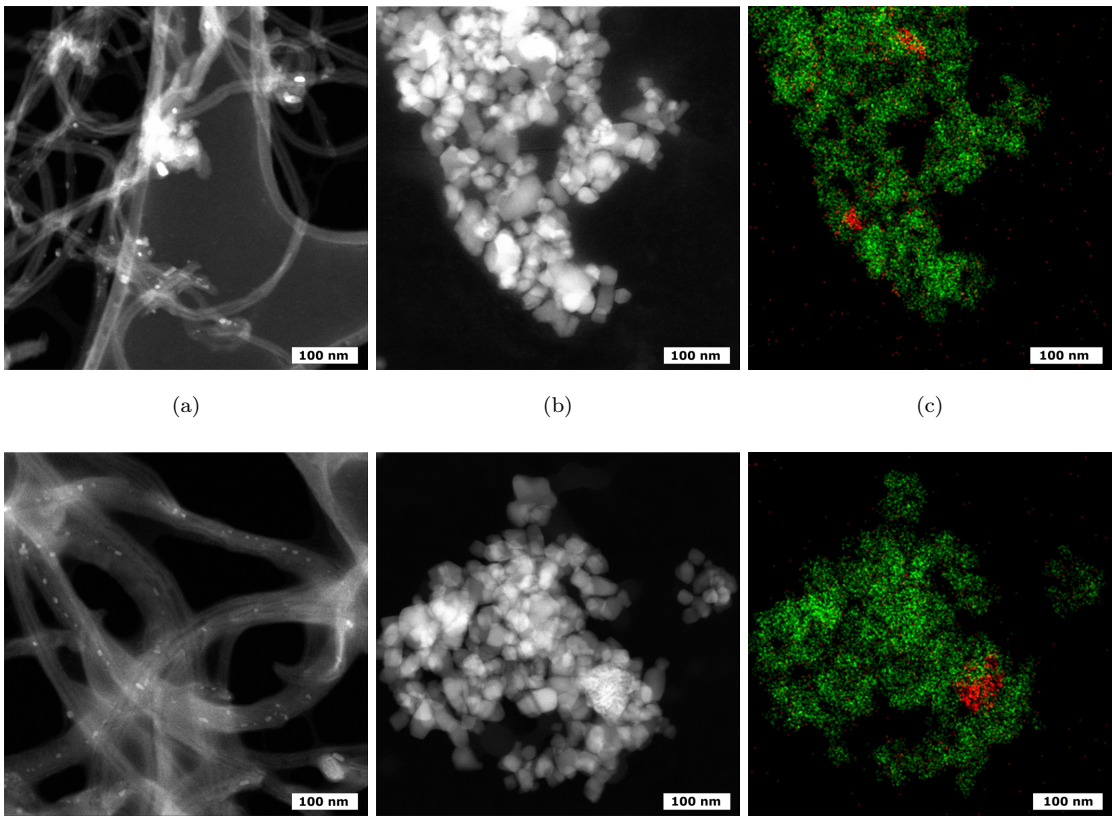

(a) (b) (c)

(d) (e) (f)

Figure 13: HAADF-STEM and HAADF-STEM-EDX images of iron nitrate nonahydrate IWI; (a) iFe/CNT-N-500-1, (b+c) iFe/TiO_2-N-350-1, (d) iFeP/CNT-N-500-1 and (e+f) iFeP/TiO_2-N-350-1. (c) and (f) are HAADF-STEM-EDX images; green indicates Ti, red indicates Fe.

3.1.2 Colloidal method

Iron NCs synthesis

Using the colloidal method, first iron nanocrystals (NCs) had to be synthesized. The iron NCs had a typical size of 7.5 nm and were spherically shaped. The resulting size and shape of the particles, however, is very sensitive to contamination of the used glassware and chemicals and to the heating rate during the synthesis. In Figure 14 TEM images of NCs are depicted where the typical hexagonal ordering of the particles and the spacing between them due to the organic ligands (oleic acid and oleylamine) can be seen. Some of the crystals are darker than others, which is due to different diffraction of the electrons on different orientations of the crystal lattices.

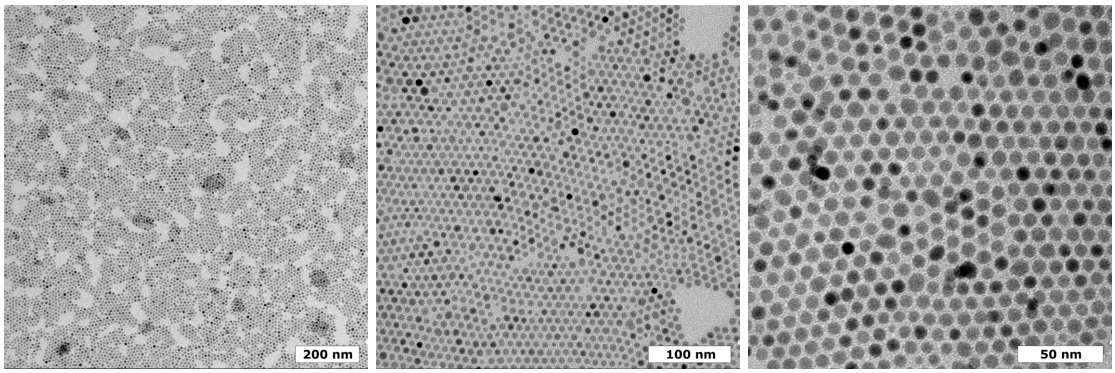

(a) (b) (c)

Figure 14: TEM images of iron nanocrystals with different scale bars; (a) 200 nm, (b) 100 nm and (c) 50 nm.

Attachment and promotion

The synthesized iron NCs were attached to the CNT and TiO_2 supports, with a maximal weight loading of 3 wt% Fe by using 800 mg support. These catalysts were analyzed with TEM and ICP-AES. With ICP-AES the weight loading of iron, sodium and sulfur on the catalysts was established, see Table 2.

Table 2: Catalyst weight loading iron NCs (wt% Fe) after attachment and after promotion and weight loading promoters (wt% Na and wt% S), as determined by ICP-AES measurements.

Catalyst	**Weight loading iron NCs (wt% Fe)**	**Weight loading promoters**	
		wt% Na	wt% S
cFe/CNT-1	3.2	–	–
cFeP/CNT-1	2.5	0.14	0.05
cFe/CNT-2	2.8	–	–
cFeP/CNT-2	2.9	0.08	0.02
cFe/CNT-3	3.4	0.02	–
cFeP/CNT-3	3.4	0.16	0.04
cFe/TiO_2-1	3.4	–	–
cFeP/TiO_2-1	2.9	0.24	0.08
cFe/TiO_2-2	3.4	–	–
cFeP/TiO_2-2	3.3	0.24	0.07
cFe/TiO_2-3	3.4	–	–
cFeP/TiO_2-3	3.3	0.23	0.08

Based on Table 2, it is shown that iron NCs and promotors were deposited on the support materials. Using CNT as support material the weight loadings of iron were around 3 wt%. When using TiO_2 as support material slightly higher iron weight loadings were obtained. This is most likely due to the lower weight of used TiO_2 support material, because the hygroscopic support was weighted undried. Both promotors were deposited on the catalysts.

After promotion of the catalysts, slight fluctuations in the iron content were measured. However, this falls in the range of the measurement error. On TiO_2 supported catalysts the sulfur content was ideal, however the sodium content was high. The solvent used for depositing the promotors was formamide with pH 7 and at this pH, which is above the point of zero charge of TiO_2 (pH_{pzc} = 6.1), the support is negatively charged. [58] It was assumed that due to electronic interactions between the TiO_2 support and the positively charged sodium atom, the weight loading of sodium on TiO_2 was higher than aimed for.

With TEM the size and shape of the iron NCs before and after attachment were determined. The attachment of the iron particles to a support had no influence on the particle shape (see Figure 15a and 15b) and little influence on the particle size (see Table 3). Moreover, due to the difference in surface areas of CNT (198 m^2/g) and TiO_2 (56 m^2/g), the inter-particle distance on TiO_2 was smaller. [59,60] After attachment, catalysts were promoted using Na_2S inorganic ligand exchange. Moreover, this promotion had no influence on the particle shape (see Figure 15c and 15d) and little influence on the particle size (see Table 3) as well. Upon promotion of the catalyst, the particles gained some mobility and ended up more clustered on the support.

In Table 3 the initial particle size and the particle size after attachment and after promotion are depicted. The average particle sizes slightly altered after attachment and after promotion, however these fluctuations were still in the range of the standard deviation.

Table 3: Initial iron oxide particle size and particle size after attachment and promotion as determined using TEM images.

Catalyst	**Particle size (nm)**		
	Before attachment	After attachment	After promotion
cFe/CNT-1	7.36 ±0.81	7.51 ±0.94	7.94 ±0.78
cFe/CNT-2	9.00 ±2.21	10.41 ±1.84	9.75 ±1.72
cFe/CNT-3	6.03 ±0.85	6.09 ±0.72	6.03 ±1.01
cFe/TiO_2-1	7.42 ±0.63	7.51 ±1.05	8.44 ±1.55
cFe/TiO_2-2	8.64 ±2.28	9.36 ±1.60	9.14 ±1.66
cFe/TiO_2-3	6.31 ±0.86	6.64 ±1.00	6.30 ±1.06

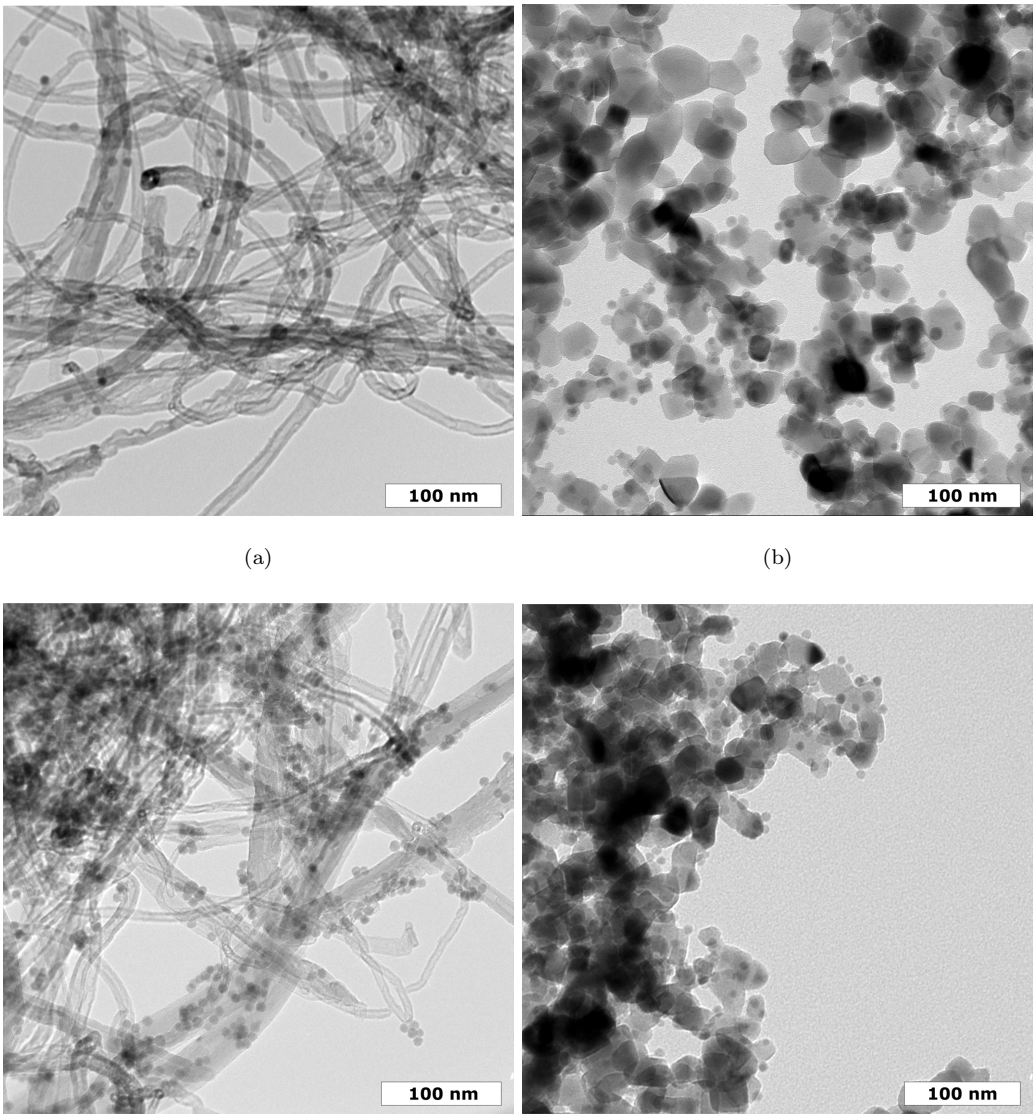

(a) (b)

(c) (d)

Figure 15: TEM images of iron NCs attached to CNT (a) cFe/CNT-1 and TiO_2 (b) cFe/TiO_2-1 and promoted with Na_2S using ligand exchange (c) cFeP/CNT-1 and (d) cFeP/TiO_2-1. The small, dark, spherical particles are the iron NCs.

3.2 Catalytic tests

3.2.1 Flowrence Test 2

The first Flowrence test is discussed in appendix B. For the second run on the Flowrence setup the following catalysts and reactor loadings were used, see Table C.1. In this test the iron nitrate nonahydrate impregnated catalysts were tested, indicated with 'N'.

In Figure 18a the FTY values for CNT supported catalysts are shown and in Figure 18b for TiO_2 supported catalysts. Data of the first 18 hours TOS is not available due to a mechanical error. In this test cFe/CNT-2 showed FTY values similar to former experiments. [47] After promotion, an increase in FTY was observed from 0.3 to 1.5 $10 \cdot 10^{-3}$ mol CO/g Fe/s after 70 hours TOS for cFeP/CNT-2 as is the same in literature. [47] The impregnated iFe/CNT-N-500-1 showed comparable FTY values to cFe/CNT-2. However, the increase in activity for iFeP/CNT-N-500-1, from 0.3 to 1.0 $10 \cdot 10^{-3}$ mol CO/g Fe/s after 70 hours TOS, was not as big as for cFeP/CNT-2. Both promoted catalyst showed deactivation during TOS, which was most likely due to particle growth. However, cFeP/CNT-2 showed more and faster deactivation than iFeP/CNT-N-500-1. All TiO_2 supported catalysts were inactive for FTO under the used conditions (10 bar, 340 °C).

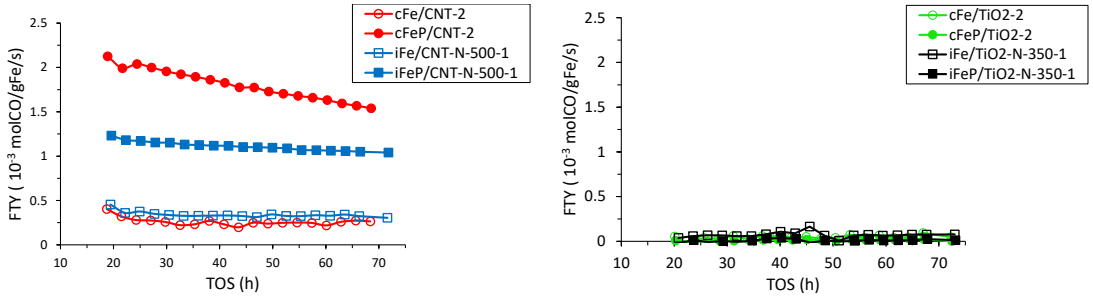

(a) (b)

Figure 16: Iron time yield (FTY) vs time on stream (TOS) of (a) cFe/CNT-2, cFeP/CNT-2, iFe/CNT-N-500-1 and iFeP/CNT-N-500-1 and (b) cFe/TiO_2-2, cFeP/TiO_2-2, iFe/TiO_2-N-350-1 and iFeP/TiO_2-N-350-1 at 340 °C, 10 bar and $H_2/CO = 2$ (open symbols: unpromoted; solid symbols: promoted; spheres: colloidal method; cubes: IWI).

For the CNT supported catalysts the product selectivities were calculated. In Table 4 these product selectivities are shown. Due to a mechanical error, selectivities are given after 35 hours TOS.

Table 4: Product selectivities Flowrence Test 2 of CNT supported catalysts after 35 hours TOS.

Catalyst	Selectivity (%c)		
	CH_4	C_2-C_4 olefins	C_{5+}
cFe/CNT-2	53	29	2
cFeP/CNT-2	15	37	10
iFe/CNT-N-500-1	50	22	3
iFeP/CNT-N-500-1	9	44	11

As can be seen in Table 4, after promotion the methane selectivity decreases and the olefin selectivity increases, for both cFeP/CNT-2 and iFeP/CNT-N-500-1. However, iFeP/CNT-N-500-1 shows slightly better product selectivities.

Spent catalysts Test 2

Because of the inactivity of the TiO_2 supported catalysts, the spent catalysts were analyzed with TEM, HAADF-STEM and HAADF-STEM-EDX. In Figure 17 cFe/TiO_2-2-spent can be seen. Most of the colloidal iron NCs had sintered into long rod like particles of 200 to 300 nm. This unexpected particle shape, in stead of big spherical like particles, was most likely due to magnetic interaction between mobile iron particles on TiO_2 at 340 °C. [27] Furthermore, some of the iron particles seemed to have been integrated into the titania support, most probably due to the SMSI.

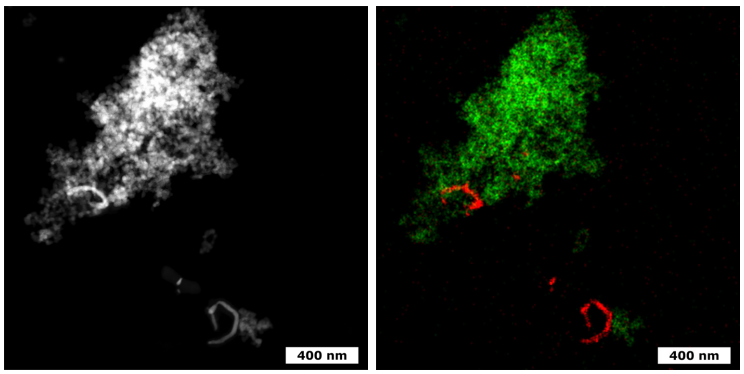

(a) (b)

Figure 17: (a) HAADF-STEM image and (b) HAADF-STEM-EDX image of cFe/TiO_2-2-spent. Green indicates Ti, red indicates Fe.

In Figure 18 cFeP/TiO_2-2-spent can be seen with a zoom in of a colloidal particle. The particles had grown and several core-shell particles had been formed which indicated the reduction of the iron oxide NCs. The iron oxide NCs were reduced *in situ* to metallic iron and after the reaction the outer layer of the particles were re-oxidized to iron oxide. Based on Mössbauer studies in literature, core-shell particles on CNT indicated the formation of the active iron carbide phase. [36] However, cFeP/TiO_2-2 was not active for FTO. A reason for this could be the high sodium content (0.24 wt% Na) which poisoned the catalyst or no carbidization of the iron.

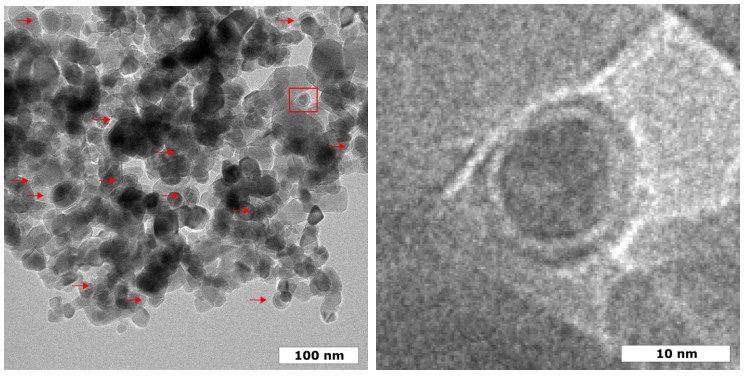

(a) (b)

Figure 18: (a) TEM image of cFeP/TiO_2-2 with core-shell particles indicated with red arrows and (b) TEM-zoom image of core-shell particle.

In Figure 19a cFe/CNT-2-spent can be seen and in Figure 19b cFeP/CNT-2-spent with in 19c a zoom-in of a core-shell particle. The particles had grown and elongation of the particles had occurred. On cFeP/CNT-2-spent several core-shell particles were formed which indicated the reduction of iron oxide and probably the formation of the active iron carbide phase.

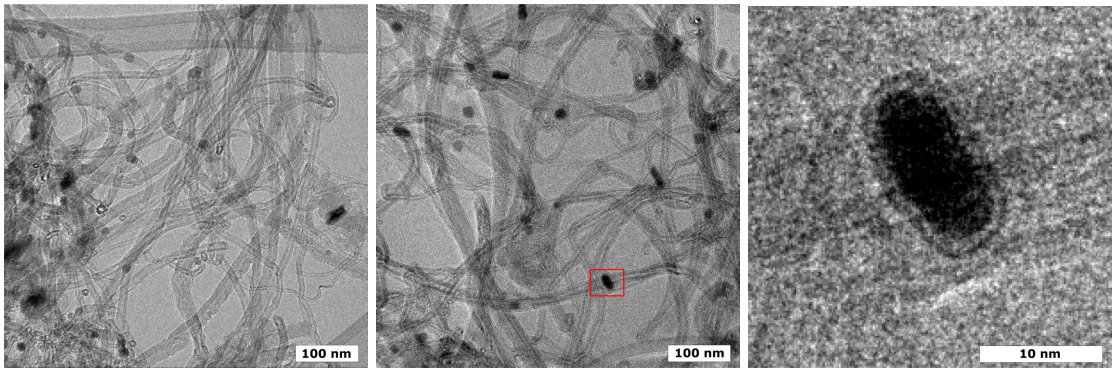

(a) (b) (c)

Figure 19: TEM images of (a) cFe/CNT-2-spent, (b) cFeP/CNT-2-spent and (c) TEM-zoom image of core-shell particle.

In Figures 20a and 20b iFe/TiO_2-N-350-1-spent can be seen and in Figures 20c and 20d iFeP/TiO_2-N-350-1-spent. All particles grew extensively due to sintering and more iron was integrated into the support material. In Figure 21a iFe/CNT-N-500-1-spent and in Figure 21b iFeP/CNT-N-500-1-spent can be seen. All particles grew and the broad particle size distribution was remained.

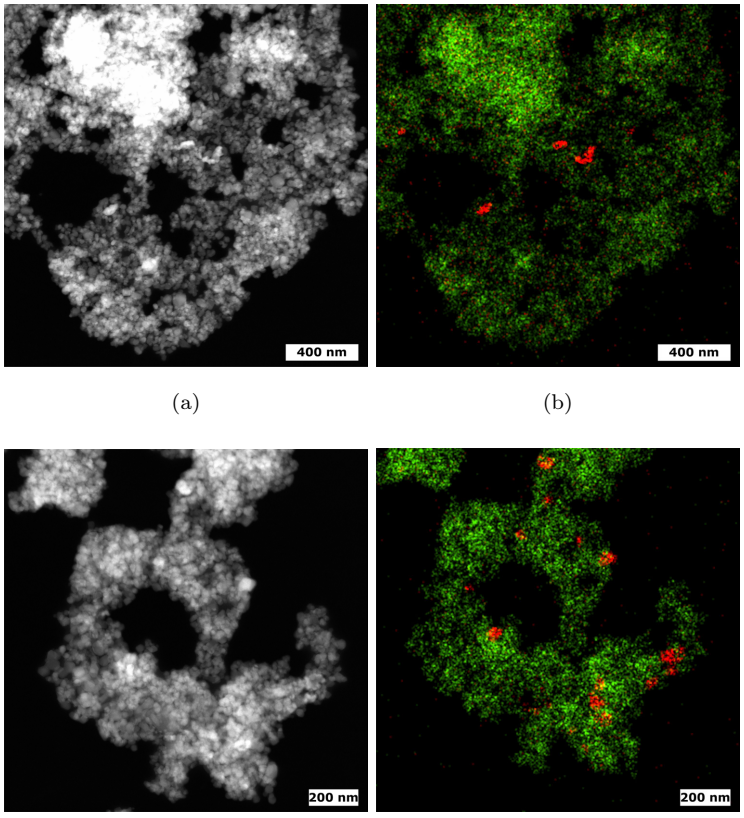

(a) (b)

(c) (d)

Figure 20: HAADF-STEM and HAADF-STEM-EDX images of (a+b) iFe/TiO_2-N-350-1-spent and (c+d) iFeP/TiO_2-N-350-1-spent. (b) and (d) are HAADF-STEM-EDX images; green indicates Ti, red indicates Fe.

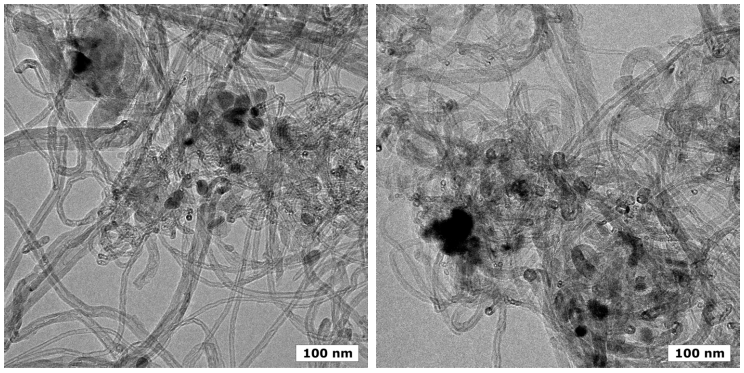

(a) (b)

Figure 21: TEM images of (a) iFe/CNT-N-500-1-spent and (b) iFeP/CNT-N-500-1-spent.

In Table 5 the particle sizes of the fresh and spent catalysts are shown. With the colloidal method, a narrow particle size distribution was obtained on the fresh catalysts. After reaction, the particles grew and the size distribution became larger. Interestingly, on cFe/TiO_2-2 long rod like particles were formed. However, using IWI the particle size distribution before and after the reaction were larger. With promotors, the particles grew more extensively due to severe sintering. From literature it is known that promotors lead to formation of mobile iron phases which result in a higher degree of particle growth. [36]

Table 5: Particle sizes of the fresh and spent catalysts (Test 2).

Catalyst	**Particle size (nm)**	
	Fresh	**Spent**
cFe/CNT-2	10.41 ±1.84	14.48 ±6.10
cFeP/CNT-2	9.75 ±1.72	19.68 ±6.65
iFe/CNT-N-500-1	3 - 20	20 - 40
iFeP/CNT-N-500-1	3 - 18	20 - 40
cFe/TiO_2-2	9.36 ±1.60	–
cFeP/TiO_2-2	9.14 ±1.66	23.44 ±7.52
iFe/TiO_2-N-350-1	20 - 60	$>$ 70
iFeP/TiO_2-N-350-1	20 - 60	$>$ 80

3.2.2 Flowrence Test 3

Due to the inactivity of all the TiO_2 supported catalysts and the massive sintering of the colloidal particles on cFe/TiO_2-2, lower reaction temperatures were used during Flowrence Test 3. Reduction and carbidization were performed at 240 ℃ and the reaction was done at 240, 260, 280 and 300 ℃ subsequently. In Figure 22 the FTY values of the catalysts can be seen.

In Figure 22a the FTY values of all CNT supported catalysts can be seen. At 240 and 260 ℃, cFe/CNT-3 was not active. However, at 280 ℃ activation occurred leading to a FTY value $0.08{\cdot}10^{-3}$ mol CO/g Fe/s. At 300 ℃the activity increased further to a final FTY value of $0.18{\cdot}10^{-3}$ mol CO/g Fe/s after 110 hours TOS, comparable to the activity of cFe/CNT-2 at 340 ℃. With promotors, cFeP/CNT-3, the catalyst activated at 240 and 260 ℃. However, after a steep increase in activity at the end of the 260 ℃ temperature range, severe deactivation occurred at 280 ℃ and activity loss compared to cFe/CNT-3. At 300 ℃ the activity slightly increased to a FTY value of $0.05 \cdot 10^{-3}$ mol CO/g Fe/s after 110 hours TOS, however this was still below the FTY value of cFe/CNT-3. These results indicated a temperature dependent promotion of colloidal iron nanoparticles supported on CNT.

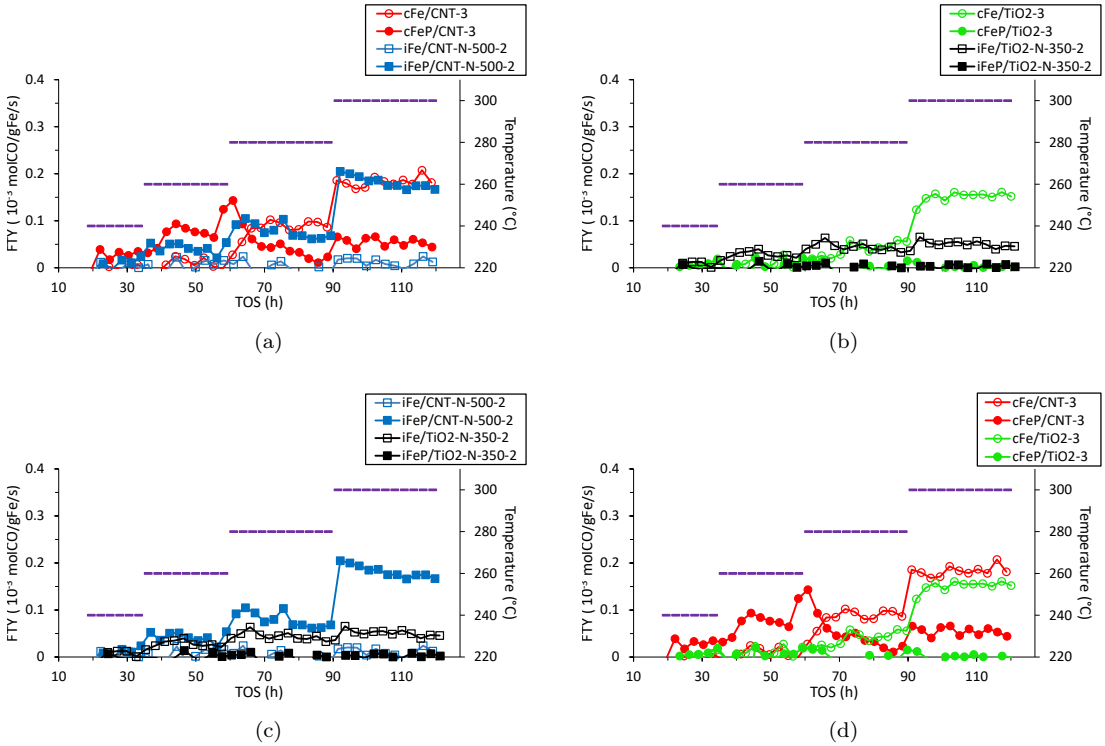

Figure 22: Iron time yield (FTY) and temperature vs time on stream (TOS) of (a) CNT supported catalysts (cFe/CNT-3, cFeP/CNT-3, iFe/CNT-N-500-2 and iFeP/CNT-N-500-2), (b) TiO_2 supported catalysts (cFe/TiO_2-3, cFeP/TiO_2-3, iFe/TiO_2-N-350-2 and iFeP/TiO_2-N-350-2), (c) catalysts obtained with IWI (iFe/CNT-N-500-2, iFeP/CNT-N-500-2, iFe/TiO_2-N-350-2 and iFeP/TiO_2-N-350-2) and (d) catalysts obtained with colloidal method (cFe/CNT-3, cFeP/CNT-3, cFe/TiO_2-3 and cFeP/TiO_2-3).

The impregnated catalyst, iFe/CNT-N-500-2, was inactive for FTO at these temperatures. However, the promoted catalyst, iFeP/CNT-N-500-2, activated at 260 °C and showed comparable FTY values to cFe/CNT-3 at 280 and 300 °C. At 300 °C the initial FTY value of iFeP/CNT-N-500-2 was slightly higher than for cFe/CNT-3, namely $0.20 \cdot 10^{-3}$ mol CO/g Fe/s after 90 hours TOS, but due to deactivation of the catalysts, the final FTY value was $0.17 \cdot 10^{-3}$ mol CO/g Fe/s after 110 hours TOS.

In Figure 22b the FTY values of all TiO_2 supported catalysts can be seen. Similar to cFe/CNT-3, cFe/TiO_2-3 activated at 280 °C at and 300 °C a FTY value of $0.16 \cdot 10^{-3}$ mol CO/g Fe/s was obtained after 110 hours TOS. This value was slightly lower than of cFe/CNT-3 at 300 °C, however still very comparable as can be seen in Figure 22d . With promotors, cFeP/TiO_2-3, the catalyst was inactive for FTO. The impregnated catalyst, iFe/TiO_2-N-350-2, activated at 260 °C and with temperature increase the activity slightly increased. At the end of the 280 °C temperature range a FTY value of $0.03 \cdot 10^{-3}$ mol CO/g Fe/s after 80 hours TOS was obtained and at the end of the 300 °C temperature range a FTY value of $0.05 \cdot 10^{-3}$ mol CO/g Fe/s after 110 hours TOS. During the temperatures ranges slight deactivation occurred for this catalyst. The promoted catalyst, iFeP/TiO_2-N-350-2, was inactive for FTO. Based on these results and the results obtained during Flowrence test 2, sodium and sulfur promotors seemed to have poisoned the TiO_2 supported catalysts; all promoted TiO_2 supported catalysts were inactive for FTO, independent of deposition method or temperature.

In Table 6 the selectivities of the active catalysts are shown at 300 ℃ after 110 hours TOS. It can be seen that for cFeP/CNT-3 the methane selectivity was decreased. However, the olefin selectivity of cFeP/CNT-3 did not increase after promotion and even slightly decreased. This adds to the observation of temperature dependent promotion of colloidal iron particles supported on CNT. Moreover, an increase in C_{5+} selectivity was observed, due to the promotors and the more FT reaction conditions (leading to longer hydrocarbons). However, for iFeP/CNT-N-500-2, the lower olefin selectivity did increase compared to cFe/CNT-3 and the C_{5+} selectivity only increased with 5%c. Similar to the results of Flowrence test 2, iFeP/CNT-N-500-2 showed better product selectivities compared to cFeP/CNT-3. Of the TiO_2 supported catalysts, only the unpromoted catalysts can be compared in terms of selectivity due to the inactivity of the promoted catalysts. The product selectivities of cFe/TiO_2-3 and iFe/TiO_2-N-350-2 were very similar, however cFe/TiO_2-3 showed slightly better product selectivities. Comparing cFe/CNT-3 and cFe/TiO_2-3, the product selectivities were comparable, though cFe/CNT-3 showed slightly better selectivities.

Table 6: Product selectivities Flowrence Test 3 at 300 ℃ after 110 hours TOS.

Catalyst	Selectivity (%c)		
	CH_4	C_2-C_4 olefins	C_{5+}
cFe/CNT-3	17	24	44
cFeP/CNT-3	3	18	73
iFe/CNT-N-500-2	–	–	–
iFeP/CNT-N-500-2	5	37	49
cFe/TiO_2-3	21	21	43
cFeP/TiO_2-3	–	–	–
iFe/TiO_2-N-350-2	22	17	47
iFeP/TiO_2-N-350-2	–	–	–

Spent catalysts Test 3

In Figure 23 HAADF-STEM and HAADF-STEM-EDX images are shown of cFe/TiO_2-3-spent and cFeP/TiO_2-3. At lower reaction temperatures, most of the colloidal iron particles on TiO_2 were stable and did not sinter, however some particles of 35 and 60 nm were obtained and some particles were integrated into the TiO_2 support. With promotors the particles showed severe sintering. This particle growth, in combination with possible poisoning of the catalysts due to the promotors, decreased the activity of promoted colloidal iron particles on TiO_2 in FTO to zero. Again, core-shell particles had formed, indicating successful reduction of the iron oxide.

In Figure 24 STEM images of cFe/CNT-3-spent and cFeP/CNT-3-spent are shown. Most of the colloidal particles on CNT showed slight growth, however some particles of approximately 70 nm were obtained, and with promotors the colloids sintered severe. Moreover, core-shell particles had formed and some promoted particles with sizes of approximately 40, 50 and 60 nm were observed. This particle growth reduced the activity of cFeP/CNT-3, however the average spent particle size did not differ much with cFeP/CNT-2-spent, a very active catalyst. This adds to the indication that promotion of colloidal iron particles on CNT was temperature dependent.

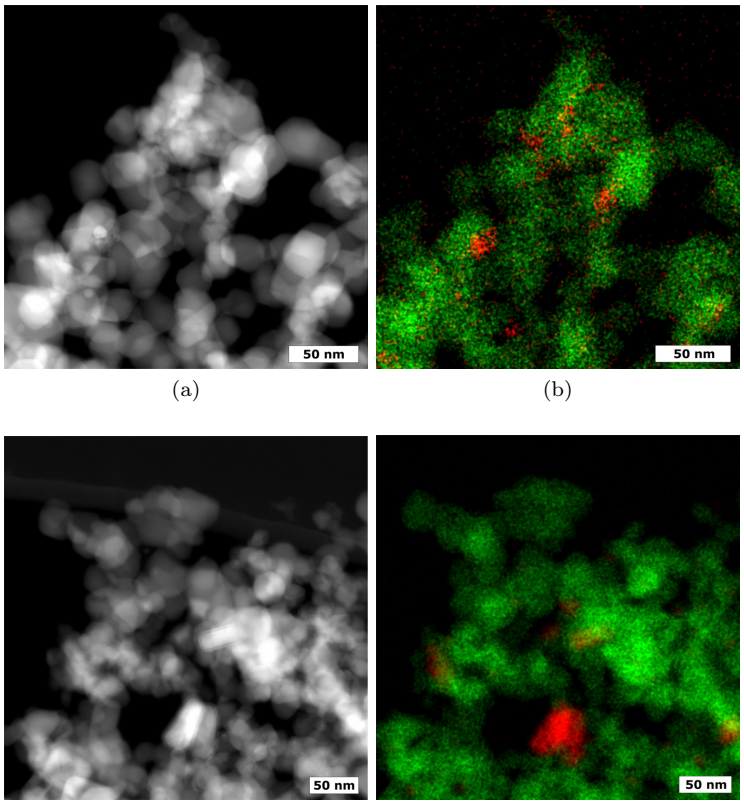

(a) (b)

(c) (d)

Figure 23: HAADF-STEM and HAADF-STEM-EDX images of (a+b) cFe/TiO_2-3-spent and (c+d) cFeP/TiO_2-3-spent. (b) and (c) are HAADF-STEM-EDX images; green indicates Ti, red indicates Fe.

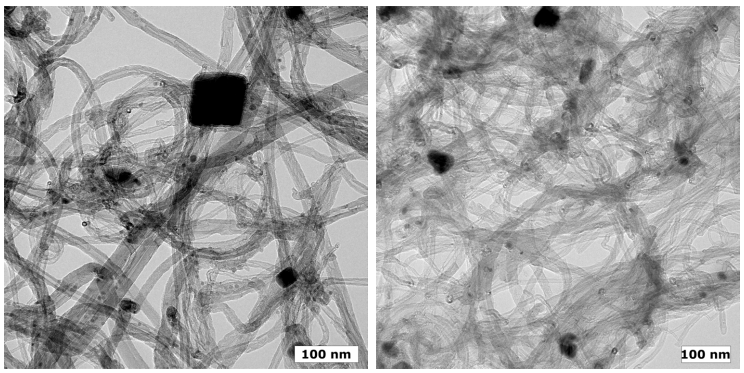

(a) (b)

Figure 24: STEM images of (a) cFe/CNT-3-spent and (b) cFeP/CNT-3-spent.

In Table 7 the average iron particle sizes of the fresh and spent catalysts are showed. The colloidal iron particles were more sinter resistant, similar to the spent catalysts of Test 2. For cFe/$TiO_2$3-spent, the few large particles were not taken into account in the standard deviation. With promotors, the colloidal particles grew more extensive to a average particle size three or four times the initial particle size. The impregnated catalysts showed severe growth and broad particle size distributions were obtained. However, on iFe/TiO_2-N-350-2-spent no more iron particles were observed and all iron most likely integrated into the support. Though, iFe/TiO_2-N-350-2 was active in FTO and showed no severe deactivation, indicating that iron particles had to be present. Analyzing spent catalysts with HAADF-STEM and HAADF-STEM-EDX gives only a representation of part of the catalyst.

Table 7: Particle sizes of the fresh and spent catalysts (Test 3).

Catalyst	**Particle size (nm)**	
	Fresh	**Spent**
cFe/CNT-3	6.09 ±0.85	9.68 ±13.93
cFeP/CNT-3	6.03 ±1.01	20.72 ±15.93
iFe/CNT-N-500-2	20 - 30	20 - 40
iFeP/CNT-N-500-2	5 - 15	20 - 40
cFe/TiO_2-3	6.64 ±1.00	6.60 ±2.91
cFeP/TiO_2-3	6.30 ±1.06	23.30 ±9.31
iFe/TiO_2-N-350-2	20 - 30	-
iFeP/TiO_2-N-350-2	40 - 60	50 - 100

4 Conclusion

Colloidal iron oxide nanoparticles with a size of approximately 7 nm were synthesized and in a second step attached on carbon nanotubes (CNT) or TiO_2. Promotors were introduced using inorganic ligand exchange with Na_2S. On TiO_2, more sodium was deposited after promotion due to the electronic interaction between the negatively charged support and positively charged sodium. The particles gained some mobility during promotion and ended up somewhat more clustered on the support material. However, the promotors did not influence the particle size or shape.

Ammonium iron citrate and iron nitrate nonahydrate were used as precursors for IWI on CNT or TiO_2. Promotors were introduced via co-impregnation. Because of the poor particle formation and distribution on TiO_2 using ammonium iron citrate as precursor, iron nitrate nonahydrate as precursor was studied. After calcination for 2 hours at 500 ℃, iron particles with a size between 3 and 20 nm were formed on CNT. On TiO_2, after calcination for hours at 350 ℃, big particles had formed with sizes between 20 and 60 nm. Moreover, as for ammonium iron citrate, several areas with iron integrated into the TiO_2 support were obtained most probably due to the SMSI. Catalyst performance was carried out on a Flowrence Avantium under industrially relevant conditions. Unfortunately, all TiO_2 supported catalysts were inactive under the used reaction conditions and showed no activity in FTO. Colloidal iron nanoparticles on CNT showed an FTY of $0.3 \cdot 10^{-3}$ mol CO/g Fe/s and with promotors this activity increased to $1.5 \cdot 10^{-3}$ mol CO/g Fe/s. Moreover, the selectivity towards methane decreased and towards lower olefins increased. The impregnated CNT showed comparable activity to colloidal iron nanoparticles on CNT. However, with promotors the activity of the impregnated catalysts increased only to $1.0 \cdot 10^{-3}$ mol CO/g Fe/s. The product selectivity of this catalyst was slightly better than of promoted colloidal particles on CNT, however the activity did not increase as much.

Analysis of the spent catalysts with STEM and STEM-EDX showed that colloidal particles on CNT were mostly sinter resistant. With promotors, the colloidal particles sintered more extensively and the initial particle size was doubled. During TOS, the promoted catalysts showed deactivation, probably due to particle growth and loss of active metal surface area. The impregnated catalysts on CNT showed severe sintering of the particles and a broader particle size distribution was obtained than with colloidal particles. The impregnated catalysts on TiO_2 showed severe particle sintering as well and more iron integrated into the TiO_2 support. The colloidal iron particles on TiO_2 showed extensive sintering into rod like particles of 200 to 300 nm. This remarkable shape was most likely the result of magnetic interaction between mobile iron particles. Even though the spent catalyst of colloidal iron particles on TiO_2 showed core-shell particles, indicating reduction was successful, this catalyst showed no activity in FTO most probably due to poisoning of the catalyst with the promotors and particle growth.

As TiO_2 supported catalysts showed no activity in FTO lower reduction, carbidization and reaction temperatures were used during a follow-up Flowrence run. Temperatures were chosen as low as possible, starting with low temperature Fischer-Tropsch conditions at 240 ℃, increasing the temperature with 20 ℃ if no activity was found within 25 hours. Colloidal iron particles on CNT activated at 280 ℃ and showed comparable activities at 300 ℃ and 340 ℃. With promotors, a loss in activity was obtained at 280 and 300 ℃. Moreover, the methane selectivity was decreased, however, the olefin selectivity was slightly decreased as well. Due to the lower reaction temperatures which result in more FT conditions and products, the C5+ selectivity increased compared to the reaction at 340 C and with promotors increased further. These results indicated a temperature dependent promotions of colloidal iron particles on CNT. The impregnated catalyst on CNT showed no activity in FTO. However, with promotors the catalyst showed comparable activity to colloidal iron particles on CNT and a better product selectivity. Compared to unpromoted colloidal iron particles on CNT, the methane selectivity decreased, the lower olefin selectivity increased and the C_{5+} selectivity increased with only 5%c, instead of 29%c.

Colloidal iron particles on TiO_2 activated at 280 ℃ and at 300 ℃ showed comparable activity to colloidal iron particles on CNT at 300 and 340 ℃. However, with promotors the colloidal iron particles on TiO_2 were inactive in FTO. Moreover, the impregnated catalysts on TiO_2 with promotors was inactive as well. These results indicated that sodium and sulfur promotors on TiO_2 supported catalysts work differently than for CNT supported catalysts and most probably poison the catalyst. The impregnated catalyst on TiO_2 without promotors activated at 260 ℃ and at 300 ℃ showed activity 5 times lower than of colloidal iron particles on TiO_2. Moreover, the product selectivity of colloidal iron particles on TiO_2 was slightly better than of the impregnated catalyst on TiO_2.

After analyzing the spent catalysts with STEM and STEM-EDX, it was found that colloidal particles on CNT showed slight growth while promoted colloids sintered severe to more than three times the initial particle size. This extensive particle growth most probably explained the loss in activity in FTO. Most of the colloidal particles on TiO_2 were stable and did not sinter, however some particles of 35 nm were observed and some particles integrated into the TiO_2 support. With promotors, the colloidal particles sintered to almost four times the initial particle size. Besides the possible poisoning of the promoted catalysts on TiO_2, the particle growth decreased the activity as well. All impregnated catalysts showed extensive sintering of the iron particles and more iron was integrated into the support of TiO_2 supported catalysts.

Thus, at 300 ℃, colloidal iron particles on TiO_2 showed comparable activity in FTO to colloidal iron particles on CNT at 300 and 340 ℃ and higher activity compared to the impregnated catalyst on TiO_2. The colloids on TiO_2 were relatively stable at this temperature and most particles did not sinter. Moreover, the product selectivity of colloidal iron particles on TiO_2 was slightly better than of the impregnated catalyst.

5 Outlook

Based on the results obtained during this project, several ideas for future experiments can be established. First, it would be useful to perform Mössbauer spectroscopy on colloidal iron nanoparticles supported on TiO_2, with and without promotors, to determine the iron phases present during the FTO reaction under the conditions used in the experiments. To gain more insight in the product selectivities and influence of the promotors at different temperatures, experiments should be performed at 1 bar with a CO conversion <1%. However, for colloidal iron nanoparticles on TiO_2 this was quite challenging.

At 300 ℃ the colloidal particles on TiO_2 were more stable and did not sinter as severe compared to the colloidal particles after reaction at 340 ℃. However, some particles were integrated into the support material. To reduce the integration of colloidal iron particles into the TiO_2 support, first impregnation and calcination of the support with an iron precursor and second attachment of colloidal iron particles could work. In this way, the surface of the TiO_2 support would be more saturated with iron due to the extensive uptake of iron into the support using IWI and probably reduce the interaction between the support and colloidal iron particles. However, a higher iron weight loading would be obtained in this way.

Further research can be done on the influence of initial colloidal particle size on the sintering of the particles on TiO_2 at different temperatures. The colloidal particles which sintered extensively at 340 ℃ on TiO_2, had a larger average initial particle size of approximately 9 nm. The colloidal particles which were tested at 300 ℃ and showed to be more stable, had an average initial particle size of approximately 6.5 nm. To exclude particle size effects on the sintering of colloidal iron particles on TiO_2, particles with sizes ranging from approximately 5 to 15 nm could be tested at different reaction temperatures.

On CNT, IWI provided a convenient reference catalyst. However, IWI on TiO_2 obtained broad particle size distributions, large particles compared to colloidal iron nanoparticles and much integration of iron into the TiO_2 support. To obtain better particle formation on TiO_2 with IWI, addition of acid HNO_3 to the iron nitrate nonahydrate precursor solution could help. In this way the iron precursor should not precipitate via iron hydroxides, forming a layer on the support, but rather form particles upon drying.

The addition of promotors with inorganic Na_2S ligand exchange on colloidal iron particles supported on TiO_2 obtained high sodium weight loadings. This high concentration of sodium, or the presence of sulfur and sodium at all, probably poisoned the catalyst. To improve the introduction of promotors on colloidal iron particles supported on TiO_2, the colloidal particles could be promoted first and attached afterwards. In this way, there is more control on the ligand exchange and no additional sodium is deposited on the support material. However, this could induce a poorer dispersion of the particles over the support material. Moreover, adjusting the concentration of promotors on colloidal iron particles supported on TiO_2 and using different promotors is interesting to study as well.

Interesting to study further, is the temperature dependent promotion of colloidal iron nanoparticles on CNT. It would be interesting to see if the promotors could increase the activity again when going from 300 to 340 ℃, expanding the low temperatures FT run. This would give more information on the working of the promotors and the location of the atoms. If the activity would increase at 340 ℃ to the value obtained in Flowrence test 2, reaction at 340 ℃, the promotion is temperature dependent. However, if the activity is not increased to the initial value, this could be an indication of migration of the promotors from the colloidal particles to the support material and decreasing the proximity of the promotors and particles. To enhance the catalytic properties of the colloidal iron particles, the promotors should be in close proximity.

Acknowledgements

I would like to express my gratitude to several people who helped obtaining the results presented in this thesis. First of all I would like to thank my daily supervisor Nynke Krans, who helped and encouraged me during the whole project. You gave me the opportunity to make the project my own work and take my own responsibilities. Your 'door' was always open for questions and to discuss results. Thank you for all your feedback on presentations, my poster and thesis and hundreds(!) of TEM images. I really enjoyed working with you!

Furthermore, I would like to thank Marjan Versluijs-Helder for TGA-MS measurements and help with XRD, Carlos Hernández Mejía for TPR measurements and Helen de Waard and Coen Mulder for ICP measurements. I would like to thank Tom van Deelen en Lennart Weber for their help with the Flowrence, 1 bar experiments and answering all kind of questions and Lars van der Wal for being supervisor when Nynke was absent.

Special thanks go to prof. dr. ir. K. P. de Jong for the opportunity do to my master thesis at ICC and for his time and interesting, helpful input during the project. Moreover, I would like to thank dr. P. Ngene for being second examiner.

Last but not least, I would like to thank all people of the ICC group and my fellow students, who have made the past months a very nice and pleasant time with borrels, Labuitje, Christmas dinners and lunch at UMC.

References

[1] Torres Galvis, H. M.; Bitter, J. H.; Khare, C. B.; Ruitenbeek, M.; Dugulan, A. I.; de Jong, K. P. *Science* **2012**, *335*, 835–838.

[2] Torres Galvis, H. M.; de Jong, K. P. *ACS Catalysis* **2013**, *3*, 2130–2149.

[3] Lappas, A.; Heracleous, E. *Production of biofuels via Fischer-Tropsch synthesis: biomass-to-liquids*; Elsevier Ltd, 2011.

[4] Dry, M. In *Fischer-Tropsch Technology*; Steynberg, A.; Dry, M., Eds.; Elsevier B.V.: Amsterdam, 2004; Vol. 152, pp 196–257.

[5] Maitlis, P. M.; de Klerk, A. *Greener Fischer-Tropsch Processes for Fuels and Feedstocks*; Maitlis, P. M.; de Klerk, A., Eds.; Wiley-VCH Verlag GmbH & Co. KGaA: Weinheim, Germany, 2013.

[6] van der Laan, G. P.; Beenackers, A. A. C. M. *Catalysis Reviews* **1999**, *41*, 255–318.

[7] Bukur, D. B.; Todic, B.; Elbashir, N. *Catalysis Today* **2016**, *275*, 66–75.

[8] Geng, S.; Jiang, F.; Xu, Y.; Liu, X. *ChemCatChem* **2016**, *8*, 1303–1307.

[9] Rayner, M. K.; Billing, D. G.; Coville, N. J. *Acta Crystallographica Section B Structural Science, Crystal Engineering and Materials* **2014**, *70*, 498–509.

[10] Claeys, M.; van Steen, E. In *Fischer-Tropsch Technology*; Steynberg, A.; Dry, M., Eds.; Elsevier B.V.: Amsterdam, 2004; Vol. 152, pp 601–680.

[11] Janardanarao, M. *Industrial & Engineering Chemistry Research* **1990**, *29*, 1735–1753.

[12] Förtsch, D.; Pabst, K.; Groß-Hardt, E. *Chemical Engineering Science* **2015**, *138*, 333–346.

[13] de Smit, E.; Weckhuysen, B. M. *Chemical Society Reviews* **2008**, *37*, 2758.

[14] Cheng, J.; Hu, P.; Ellis, P.; French, S.; Kelly, G.; Lok, C. M. *Topics in Catalysis* **2010**, *53*, 326–337.

[15] Torres Galvis, H. M.; Bitter, J. H.; Davidian, T.; Ruitenbeek, M.; Dugulan, A. I.; de Jong, K. P. *Journal of the American Chemical Society* **2012**, *134*, 16207–16215.

[16] Liu, R.-J.; Xu, Y.; Qiao, Y.; Li, Z.-H.; Ma, X.-B. *Fuel Processing Technology* **2015**, *139*, 25–32.

[17] Martin-Martinez, J. M.; Vannice, M. A. *Industrial & Engineering Chemistry Research* **1991**, *30*, 2263–2275.

[18] Eggenhuisen, T. M.; De Jongh, P. E. In *Nanoparticles: Workhorses of Nanoscience*; de Mello Donegá, C., Ed.; Springer Berlin Heidelberg: Berlin, Heidelberg, 2014; pp 121–144.

[19] van Dillen, A.; Terörde, R. J.; Lensveld, D. J.; Geus, J. W.; de Jong, K. P. *Journal of Catalysis* **2003**, *216*, 257–264.

[20] Casavola, M.; Hermannsdörfer, J.; de Jonge, N.; Dugulan, A. I.; de Jong, K. P. *Advanced Functional Materials* **2015**, *25*, 5309–5319.

[21] Groeneveld, E.; de Mello-Donega, C. In *Nanoparticles: Workhorses of Nanoscience*; de Mello Donegá, C., Ed.; Springer Berlin Heidelberg: Berlin, Heidelberg, 2014; pp 145–189.

[22] Jia, C.-J.; Schüth, F. *Physical Chemistry Chemical Physics* **2011**, *13*, 2457.

[23] Tao, A. R.; Habas, S.; Yang, P. *Small* **2008**, *4*, 310–325.

[24] Vreeland, E. C.; Watt, J.; Schober, G. B.; Hance, B. G.; Austin, M. J.; Price, A. D.; Fellows, B. D.; Monson, T. C.; Hudak, N. S.; Maldonado-Camargo, L.; Bohorquez, A. C.; Rinaldi, C.; Huber, D. L. *Chemistry of Materials* **2015**, *27*, 6059–6066.

[25] LaMer, V. K.; Dinegar, R. H. *Journal of the American Chemical Society* **1950**, *72*, 4847–4854.

[26] Polte, J. *CrystEngComm* **2015**, *17*, 6809–6830.

[27] Huber, D. L. *Small* **2005**, *1*, 482–501.

[28] Kwon, S. G.; Hyeon, T. *Accounts of Chemical Research* **2008**, *41*, 1696–1709.

[29] Kharisov, B. I.; Dias, H. V. R.; Kharissova, O. V.; Vázquez, A.; Peña, Y.; Gómez, I. *RSC Adv.* **2014**, *4*, 45354–45381.

[30] Nag, A.; Kovalenko, M.; Lee, J.; Liu, W.; Spokoyny, B.; Talapin, D. *Analytical Chemistry* **2011**, *133*, 10612–10620.

[31] Moya, C.; Batlle, X.; Labarta, A. *Phys. Chem. Chem. Phys.* **2015**, *17*, 27373–27379.

[32] Nakaya, M.; Nishida, R.; Muramatsu, A. *Molecules* **2014**, *19*, 11395–11403.

[33] Guardia, P.; Labarta, A.; Batlle, X. *The Journal of Physical Chemistry C* **2011**, *115*, 390–396.

[34] Xu, Z.; Shen, C.; Hou, Y.; Gao, H.; Sun, S. *Chemistry of Materials* **2009**, *21*, 1778–1780.

[35] Hyeon, T. *Chemical Communications* **2003**, 927–934.

[36] Xie, J.; Torres Galvis, H. M.; Koeken, A. C. J.; Kirilin, A.; Dugulan, A. I.; Ruitenbeek, M.; de Jong, K. P. *ACS catalysis* **2016**, *6*, 4017–4024.

[37] Tauster, S. J.; Fung, S. C.; Garten, R. L. *Journal of the American Chemical Society* **1978**, *100*, 170–175.

[38] Bagheri, S.; Muhd Julkapli, N.; Bee Abd Hamid, S. *The Scientific World Journal* **2014**, *2014*, 1–21.

[39] de Jongh, P. E.; Eggenhuisen, T. M. In *Nanoparticles*; Springer Berlin Heidelberg: Berlin, Heidelberg, 2014; pp 99–120.

[40] Tauster, S. J.; Fung, S. C.; Baker, R. T. K.; Horsley, J. A. *Science* **1981**, *211*, 1121–1125.

[41] Tauster, S. J. *Accounts of Chemical Research* **1987**, *20*, 389–394.

[42] Santos, J.; Phillips, J.; Dumesic, J. A. *Journal of Catalysis* **1983**, *81*, 147–167.

[43] Mogorosi, R. P. **2012**.

[44] Li, D. G.; Wang, C.; Tripkovic, D.; Sun, S. H.; Markovic, N. M.; Stamenkovic, V. R. *Acs Catalysis* **2012**, *2*, 1358–1362.

[45] Torres Galvis, H. M.; Koeken, A. C.; Bitter, J. H.; Davidian, T.; Ruitenbeek, M.; Dugulan, A. I.; de Jong, K. P. *Catalysis Today* **2013**, *215*, 95–102.

[46] Xie, J.; Yang, J.; Dugulan, A. I.; Holmen, A.; Chen, D.; de Jong, K. P.; Louwerse, M. J. *ACS Catalysis* **2016**, *6*, 3147–3157.

[47] Casavola, M.; Xie, J.; Meeldijk, J. D.; Krans, N. A.; Goryachev, A.; Hofmann, J. P.; Dugulan, A. I.; Jong, K. P. D. *ACS Catalysis* **2017**, *7*, 5121–5128.

[48] Torres Galvis, H. M.; Koeken, A. C.; Bitter, J. H.; Davidian, T.; Ruitenbeek, M.; Dugulan, A. I.; de Jong, K. P. *Journal of Catalysis* **2013**, *303*, 22–30.

[49] Oschatz, M.; Lamme, W. S.; Xie, J.; Dugulan, A. I.; de Jong, K. P. *ChemCatChem* **2016**, *8*, 2846–2852.

[50] Schulz, H. In *Fischer-Tropsch Synthesis, Catalysts and Catalysis*; Davis, B.; Occelli, M., Eds.; Elsevier B.V.: Amsterdam, 2007; Vol. 163, pp 177–199.

[51] Prieto, G.; Zečević, J.; Friedrich, H.; de Jong, K. P.; de Jongh, P. E. *Nature Materials* **2012**, *12*, 34–39.

[52] Jahangiri, H.; Bennett, J.; Mahjoubi, P.; Wilson, K.; Gu, S. *Catal. Sci. Technol.* **2014**, *4*, 2210–2229.

[53] Dry, M. In *Fischer-Tropsch Technology*; Steynberg, A.; Dry, M., Eds.; Elsevier B.V.: Amsterdam, 2004; Vol. 152, pp 533–600.

[54] Smith R J, B.; Loganathan, M.; Shantha, M. S. *International Journal of Chemical Reactor Engineering* **2010**, *8*.

[55] Koeken, A. C. J.; Torres Galvis, H. M.; Davidian, T.; Ruitenbeek, M.; de Jong, K. P. *Angewandte Chemie International Edition* **2012**, *51*, 7190–7193.

[56] Casavola, M.; Xie, J.; Meeldijk, J. D.; Krans, N. A.; Goryachev, A.; Hofmann, J. P.; Dugulan, A. I.; Jong, K. P. D. *ACS Catalysis* **2017**, *7*, 5121–5128.

[57] Mahajan, A.; Kingon, A.; Kukovecz, A.; Konya, Z.; Vilarinho, P. M. *Materials Letters* **2013**, *90*, 165–168.

[58] Preocanin, T.; Kallay, N. *Croatica Chemica Acta* **2006**, *79*, 95–106.

[59] Terzyk, A. P.; Wiåniewski, M.; Dulska, K.; Bielicka, A.; Gauden, P. A.; Furmaniak, S.; Werengowska-Ciećwierz, K. *Adsorption* **2013**, *19*, 269–272.

[60] Viswanathan, B.; Raj, K. J. A. *Indian Journal of Chemistry - Section A Inorganic, Physical, Theoretical and Analytical Chemistry* **2009**, *48*, 1378–1382.

List of Figures

List of Tables

A TGA and TGA-MS

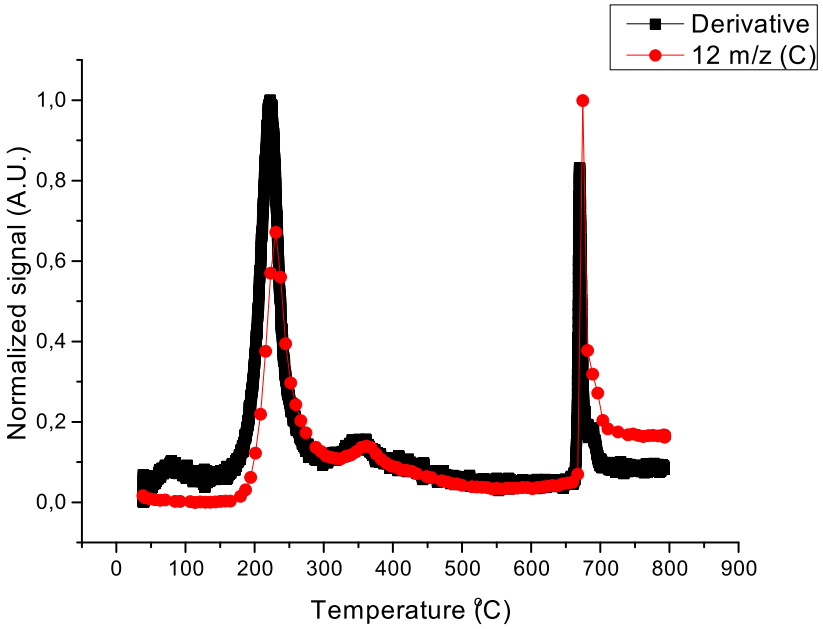

Figure A.1: Derivative of of weight loss during TGA of iFe/CNT-C-500 with the MS signal of carbon (m/z 12). Both graphs are normalized to 1.

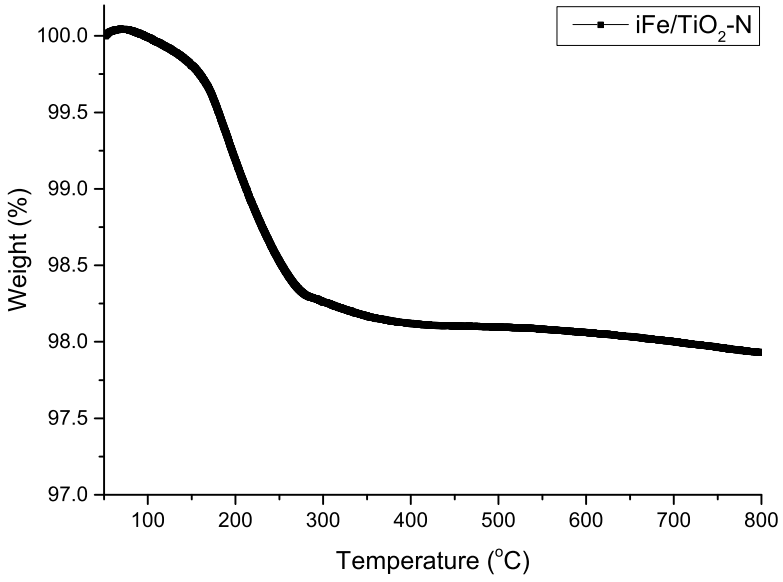

Figure A.2: TGA of the weight loss due to the decomposition of iron nitrate nonahydrate on TiO_2.

B Flowrence Test 1

For the first run on the Flowrence setup the following catalysts and reactor loadings were used, see Table B.1.

Table B.1: Reactor loading Flowrence Test 1.

Catalyst ID	Catalyst loading (mg)	SiC loading (mg)	Bed length (cm)
TiO_2	39.9	145.1	8.5
Blank	0	0	15.3
cFe/CNT-1	20.1	148.1	5.6
cFeP/CNT-1	20.2	151.6	5.5
iFe/CNT-C-500	20.7	149.9	5.6
iFeP/CNT-C-500	20.3	148.1	5.3
cFe/TiO_2-1	10.6	149.8	3.1
cFe/TiO_2-1	40.6	151.4	5.6
cFeP/TiO_2-1	16.4	153.6	3.4
iFe/TiO_2-C-250	20.3	147.2	3.2
iFe/TiO_2-C-500	10.3	149.9	3.1
iFe/TiO_2-C-500	40.5	153.1	4.2
iFeP/TiO_2-C-500	10.1	149.8	3.0
iFeP/TiO_2-C-500	40.4	149.5	4.1

Based on former experiments, a catalyst loading of 20 mg cFe/CNT was used as reference for FTO which should obtain an iron time yield (FTY) of around $10 \cdot 10^{-5}$ mol CO/g Fe/s after 60 hours time-on-stream (TOS). However, cFe/CNT-1 showed no activity for FTO under these conditions, as can be seen in Figure B.1. Based on this result this first FTO test was defined as not reliable, however the results will be discussed here.

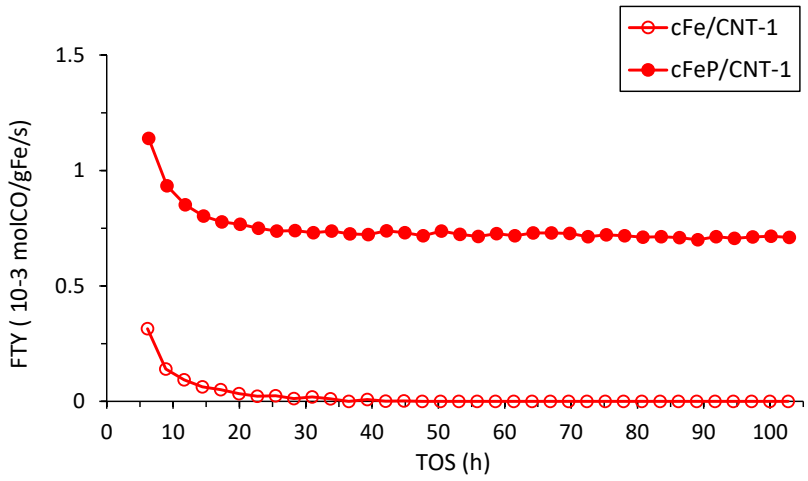

Figure B.1: FTY of cFe/CNT-1 and cFeP/CNT-1.

The FTY of cFeP/CNT-1 was similar to former experiments. After 60 hours TOS an FTY value of around $71 \cdot 10^{-5}$ mol CO/g Fe/s was obtained, as can be seen in Figure B.1. Even though the data for cFe/CNT-1 was not reliable, an increase in activity for the FTO process after promotion was observed. For both catalysts severe deactivation occurred in the first 20 hours TOS, but after this steep decrease the catalysts were stable up to 100 hours TOS.

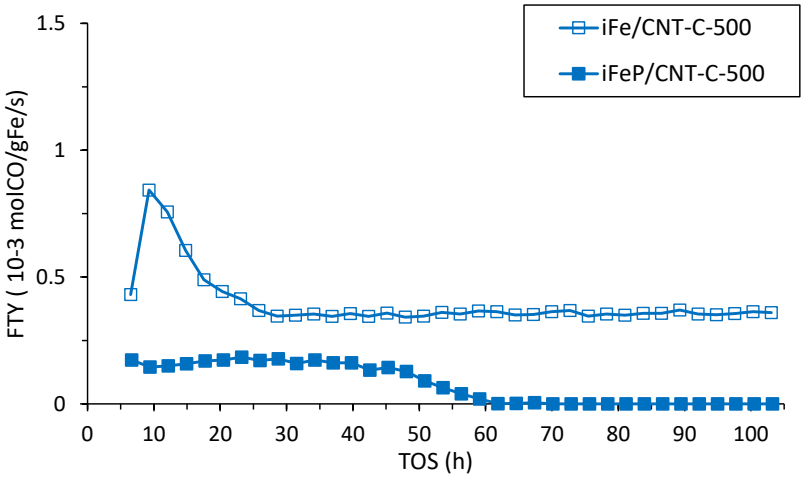

Figure B.2: FTY of iFe/CNT-C-500 and iFeP/CNT-C-500.

In Figure B.2 the FTY values for iFe/CNT-C-500 and iFeP/CNT-C-500 are shown. For iFe/CNT-C-500 a FTY value of $36 \cdot 10^{-5}$ mol CO/g Fe/s was obtained after 60 hours TOS, which was higher than for cFe/CNT-1, but this data was very unreliable. Deposition of promotors with IWI did not increase the FTO activity, as can be seen. After 60 hours TOS iFeP/CNT-C-500 was inactive, severe deactivation started already after 40 hours TOS. The massive increase in activity for iFe/CNT-C-500 during the first two measurements, from 43 to $84 \cdot 10^{-5}$ mol CO/g Fe/s, was quite remarkable. Most likely the first measurement was not reliable due to measurement issues and severe deactivation occurred in the first 30 hours TOS.

In Figure B.3 the FTY values for cFe/TiO_2-1 (40 mg catalyst loading) and iFe/TiO_2-C-250 are shown. For both catalysts severe deactivation occurred in the first 30 hours TOS. After this initial deactivation cFe/TiO_2-1 remained stable for the remaining TOS, with a FTY value between 3 and $4 \cdot 10^{-5}$ mol CO/g Fe/s and a CO conversion between 3 and 4 %. However, measurements were unreliable when the CO conversion was below 4 %. iFe/TiO_2-C-250 kept deactivating during TOS and after 75 hours TOS the activity was comparable to cFe/TiO_2-1. During the whole run the deviations of the measurements for iFe/TiO_2-C-250 were quite significant. This was most probably due to the low CO conversion of this catalyst, which decreased from 3 to 1 % between 20 and 100 hours TOS.

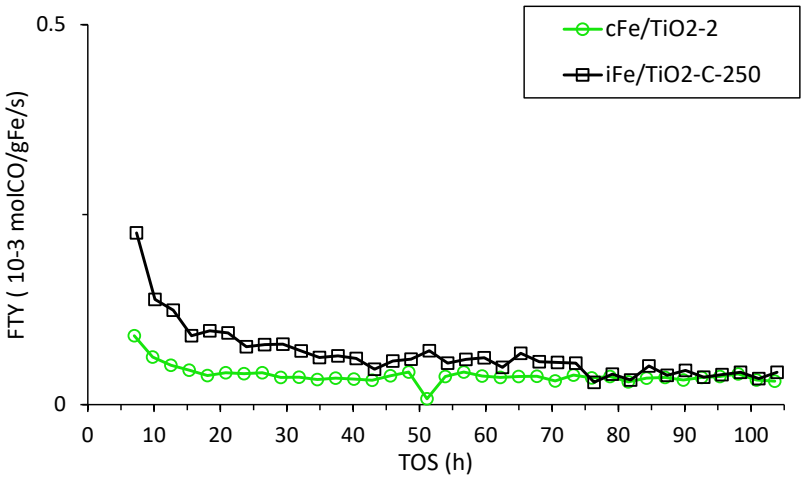

Figure B.3: FTY of cFe/TiO_2-1 and iFe/TiO_2-C-250.

The other catalysts which were tested in the Flowrence setup and not mentioned further were inactive for FTO, as can be seen in Figure B.4. To investigate this further, TEM and STEM-EDX images were made of all the spent catalysts.

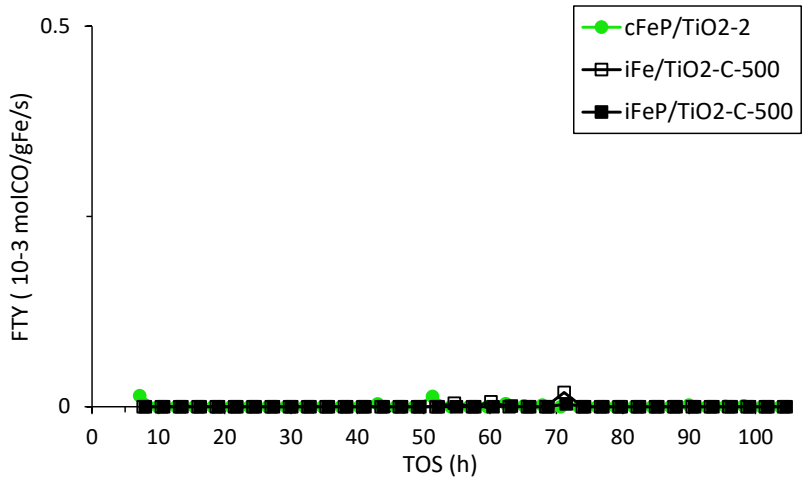

Figure B.4: FTY values of inactive catalysts in FTO; cFeP/TiO_2-1, iFe/TiO_2-C-500 and iFeP/TiO_2-C-500.

Spent catalysts Test 1

Analyzing the spent catalysts using TEM and STEM-EDX images, an increase in particle size was observed, see Table B.2.

Table B.2: Particle sizes of the fresh and spent catalysts (Test 1).

Catalyst	**Particle size (nm)**	
	Fresh	**Spent**
cFe/CNT-1	7.51 ±0.94	43.03 ±18.91
cFeP/CNT-1	7.94 ±0.78	15.65 ±4.59
iFe/CNT-C-500	5 - 15	10 - 20
iFeP/CNT-C-500	3 - 15	10 - 20
cFe/TiO_2-1	7.51 ±1.05	42.43 ±21.23
cFeP/TiO_2-1	8.44 ±1.55	21.39 ±5.47
iFe/TiO_2-C-250	-	15 - 30
iFe/TiO_2-C-500	20 - 30	30 - 40
iFeP/TiO_2-C-500	15 - 25	30 - 40

Both cFe/CNT-1 and cFe/TiO_2-1 showed a substantial increase in particle size due to sintering from 7.51 nm to around 43 nm, with a large particle size distribution. This increase was more extensive than expected, based on former studies. The promoted catalysts showed less particle growth, although promotors should enhance particle growth. The impregnated catalysts also showed an increase in particle size and sintered more than the promoted colloidal particles. On TiO_2 more iron was integrated into the support after the reaction. Based on the extensive particle growth of colloidal iron particles on CNT and TiO_2, these particles were not stable at 340 ℃. For cFe/TiO_2-2 this could explain the inactivity in FTO.

C Flowrence Test 2

Table C.1: Reactor loading Flowrence Test 2.

Catalyst ID	Catalyst loading (mg)	SiC loading (mg)	Bed length (cm)
Blank	0	0	15.5
cFe/CNT-2	20.2	155.0	3.5
cFe/CNT-2	20.3	153.9	3.3
cFeP/CNT-2	20.1	149.7	3.3
iFe/CNT-N-500-1	10.1	150.3	2.6
iFeP/CNT-N-500-1	10.2	150.8	2.3
iFe/CNT-N-500-1	30.1	150.0	3.6
iFeP/CNT-N-500-1	30.1	151.8	3.7
cFe/TiO_2-2	20.8	150.3	2.0
cFe/TiO_2-2	20.8	150.2	2.1
cFeP/TiO_2-2	30.0	150.2	2.5
cFeP/TiO_2-2	30.0	150.2	2.4
iFe/TiO_2-N-350-1	10.5	150.9	1.7
iFe/TiO_2-N-350-1	30.2	151.0	2.1
iFeP/TiO_2-N-350-1	10.5	150.0	1.8
iFeP/TiO_2-N-350-1	30.1	150.0	2.1

XRD spectra of cFe/TiO_2-2 and cFe/TiO_2-2-spent were obtained and analyzed to determine integration of iron into the TiO_2 support. Some minor differences were observed, indicated with stars in Figure C.1, which could be attributed to mixed Fe-Ti phases. Due to the low iron weight loading, no peak was observed of metallic iron. The peak at 27 degree however, could be due to Fe_2O_3. All other peaks could be subscribed to the TiO_2 P25 support, a mixture of anatase and rutile.

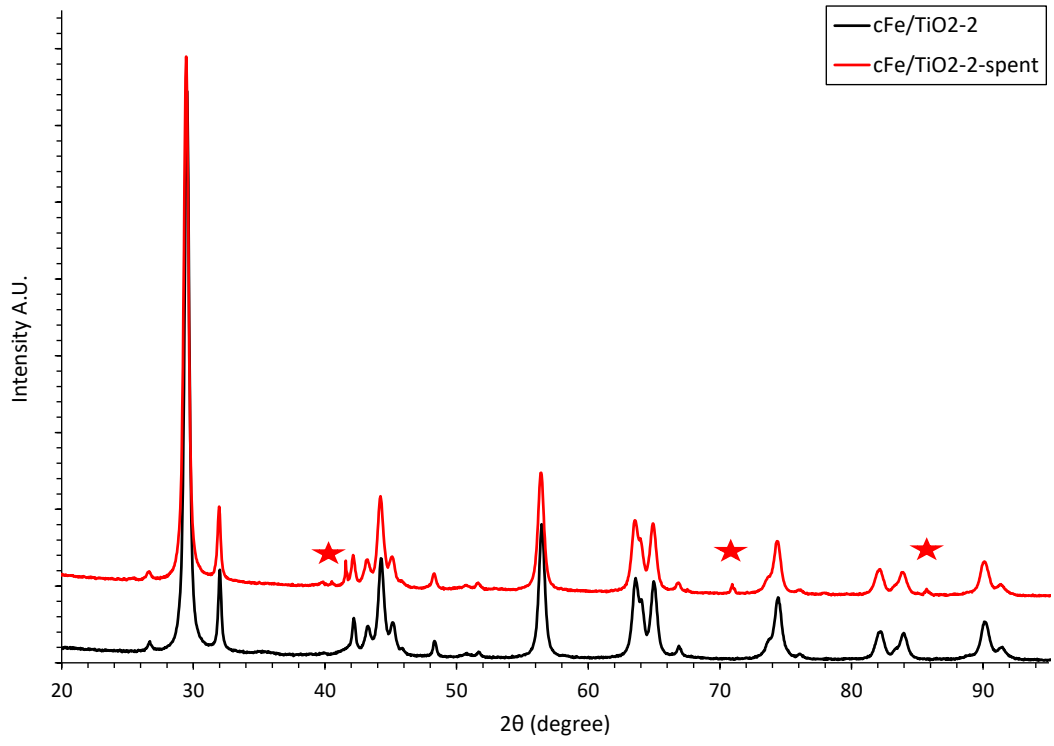

Figure C.1: XRD of cFe/TiO_2-2 and cFe/TiO_2-2-spent. Stars indicate differences.

D Flowrence Test 3

Table D.1: Reactor loading Flowrence Test 3.

Catalyst ID	**Catalyst loading (mg)**	**SiC loading (mg)**	**Bed length (cm)**
Reference	0	0	15.6
SiC	0	50.4	1.2
cFe/CNT-3	30.2	50.4	5.0
cFe/CNT-3	50.2	0	7.0
cFeP/CNT-3	30.1	50.5	5.4
cFeP/CNT-3	50.3	0	7.0
iFe/CNT-N-500-2	50.3	0	6.2
iFeP/CNT-N-500-2	50.2	0	6.4
cFe/TiO_2-2	35.3	150.5	5.4
cFe/TiO_2-2	70.2	100.2	7.5
cFeP/TiO_2-2	35.3	150.0	4.8
cFeP/TiO_2-2	70.3	50.4	5.1
iFe/TiO_2-N-350-2	35.2	150.2	4.1
iFe/TiO_2-N-350-2	70.3	100.2	4.0
iFeP/TiO_2-N-350-2	35.3	150.1	4.0
iFeP/TiO_2-N-350-2	70.3	100.3	4.1

In Figure D.1 the impregnated CNT and TiO_2 spent catalysts of Flowrence test 3 are showed.

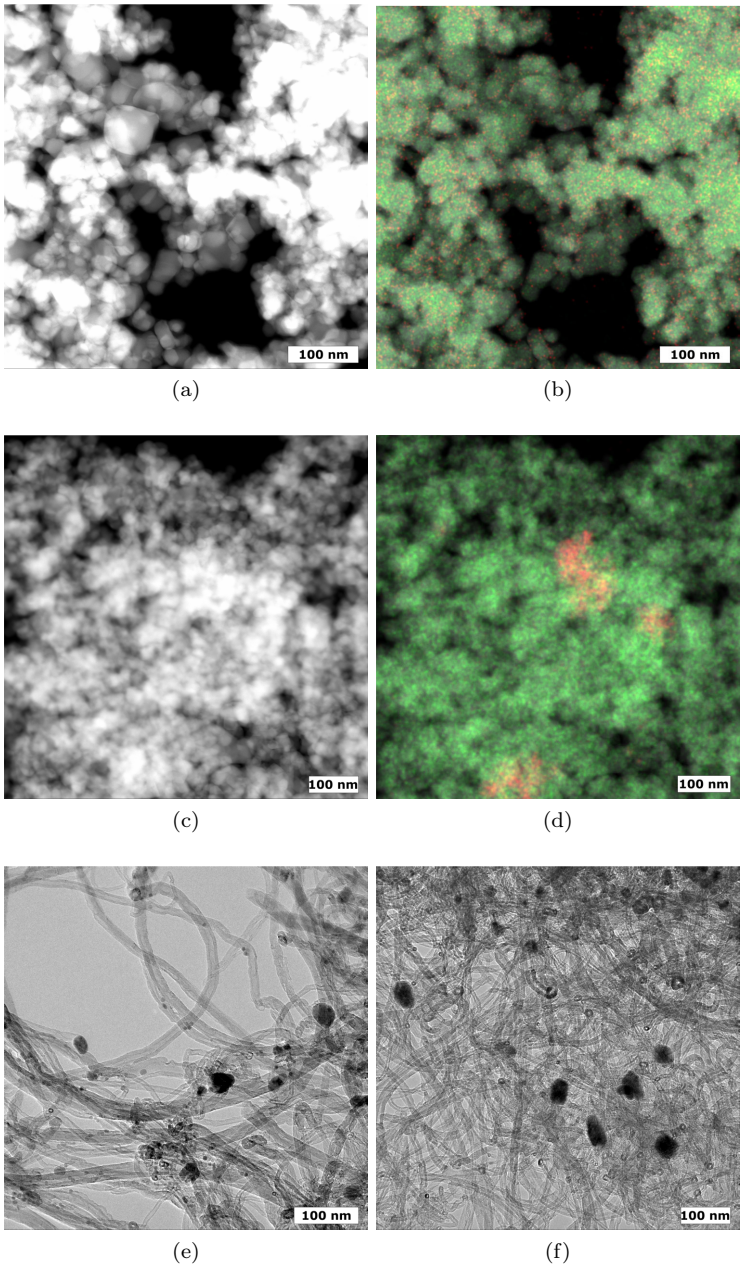

(a) (b) (c) (d) (e) (f)

Figure D.1: (a+b) HAADF-STEM and HAADF-STEM-EDX images of iFe/TiO_2-N-350-2-spent, (c+d) HAADF-STEM and HAADF-STEM-EDX images of iFeP/TiO_2-N-350-2-spent, (e) TEM image of iFe/CNT-N-500-2-spent and (f) TEM image of iFeP/CNT-N-500-2-spent. (b) and (d) are HAADF-STEM-EDX images; green indicates Ti, red indicates Fe.